Solar Physics
May 16, 2017

Observing the Sun with the Atacama Large Millimeter-submillimeter Array (ALMA): Fast-Scan Single-Dish Mapping

S.M. White[1] · K. Iwai[2] · N.M. Phillips[3,4] · R.E. Hills[5] · A. Hirota[3,6] · P. Yagoubov[7] · G. Siringo[3,4] · M. Shimojo[6] · T.S. Bastian[8] · A.S. Hales[3,8] · T. Sawada[3,6] · S. Asayama[3,6] · M. Sugimoto[6] · R.G. Marson[9] · W. Kawasaki[6] · E. Muller[6] · T. Nakazato[6] · K. Sugimoto[6] · R. Brajša[10] · I. Skokić[11] · M. Bárta[11] · S. Kim[12] · A.J. Remijan[8] · I. de Gregorio[3,4] · S.A. Corder[3,8] · H.S. Hudson[13] · M. Loukitcheva[14,15,16] · B. Chen[14] · B. De Pontieu[17] · G.D. Fleishmann[14] · D.E. Gary[14] · A. Kobelski[18] · S. Wedemeyer[19] · Y. Yan[20]

✉ S.M. White
stephen.white.24@us.af.mil

[1] Space Vehicles Directorate, Air Force Research Laboratory, 3550 Aberdeen Avenue SE, Kirtland AFB, NM 87117-5776, USA

[2] National Institute of Information and Communications Technology, Koganei 184-8795, Tokyo, Japan

[3] Joint ALMA Observatory (JAO), Alonso de Córdova 3107, Vitacura 763-0355, Santiago, Chile

[4] European Southern Observatory, Alonso de Córdova 3107, Vitacura 763-0355, Santiago, Chile

[5] Astrophysics Group, Cavendish Laboratory, JJ Thomson Avenue, Cambridge CB3 0HE, UK

[7] European Southern Observatory (ESO), Karl-Schwarzschild-Strasse 2, 85748 Garching bei München, Germany

[6] National Astronomical Observatory of Japan (NAOJ), 2-21-1 Osawa, Mitaka, Tokyo 181-8588, Japan

[8] National Radio Astronomy Observatory (NRAO), 520 Edgemont Road, Charlottesville, VA 22903, USA

[9] National Radio Astronomy Observatory (NRAO), Pete V. Domenici Science Operations Center, 1003 Lopezville Road, Socorro, NM 87801

[10] Hvar Observatory, Faculty of Geodesy, University of Zagreb, Kačićeva 26, 10000 Zagreb, Croatia

[11] Astronomical Institute, Czech Academy of Sciences, Fričova 298, 251 65 Ondřejov, Czech Republic

[12] Korea Astronomy and Space Science Institute, Daejeon 305-348, Korea

[13] School of Physics and Astronomy, University of Glasgow, Glasgow, G12 8QQ, Scotland, UK

[14] Center For Solar-Terrestrial Research, New Jersey Institute of Technology, Newark, NJ 07102, USA

[15] Max-Planck-Institut for Sonnensystemforschung, Justus-von-Liebig-Weg 3, 37077 Göttingen, Germany

[16] Astronomical Institute, St. Petersburg University, Universitetskii pr. 28, 198504, St. Petersburg, Russia

[17] Lockheed Martin Solar & Astrophysics Lab, Org. A021S, Bldg. 252, 3251 Hanover Street, Palo Alto, CA 94304, USA

[18] Center for Space Plasma and Aeronomic Research, The University of Alabama Huntsville, Huntsville, AL 35899, USA

[19] Institute of Theoretical Astrophysics, University of Oslo, Postboks 1029 Blindern, N-0315 Oslo, Norway

[20] National Astronomical Observatories, Chinese Academy of Sciences A20 Datun Road, Chaoyang District, Beijing 100012, China

Abstract The Atacama Large Millimeter-submillimeter Array (ALMA) radio telescope has commenced science observations of the Sun starting in late 2016. Since the Sun is much larger than the field of view of individual ALMA dishes, the ALMA interferometer is unable to measure the background level of solar emission when observing the solar disk. The absolute temperature scale is a critical measurement for much of ALMA solar science, including the understanding of energy transfer through the solar atmosphere, the properties of prominences, and the study of shock heating in the chromosphere. In order to provide an absolute temperature scale, ALMA solar observing will take advantage of the remarkable fast-scanning capabilities of the ALMA 12 m dishes to make single-dish maps of the full Sun. This article reports on the results of an extensive commissioning effort to optimize the mapping procedure, and it describes the nature of the resulting data. Amplitude calibration is discussed in detail: a path that utilizes the two loads in the ALMA calibration system as well as sky measurements is described and applied to commissioning data. Inspection of a large number of single-dish datasets shows significant variation in the resulting temperatures, and based on the temperature distributions we derive quiet-Sun values at disk center of 7300 K at $\lambda = 3$ mm and 5900 K at $\lambda = 1.3$ mm. These values have statistical uncertainties of order 100 K, but systematic uncertainties in the temperature scale that may be significantly larger. Example images are presented from two periods with very different levels of solar activity. At a resolution of order $25''$, the 1.3 mm wavelength images show temperatures on the disk that vary over about a 2000 K range. Active regions and plage are amongst the hotter features while a large sunspot umbra shows up as a depression and filament channels are relatively cool. Prominences above the solar limb are a common feature of the single-dish images.

Keywords: Radio emission; Chromosphere; Heating, chromospheric; Instrumentation and Data Management

1. Introduction

The earliest observations of the Sun at millimeter wavelengths were carried out with the single-dish telescopes used to develop observing at such short wavelengths, frequently treating the Sun as a calibration source (*e.g.* Sinton, 1952; Whitehurst, Copeland, and Mitchell, 1957; Coates, 1958; Tolbert and Straiton, 1961). Subsequently, more attention was paid to understanding what the observations were telling us about the solar atmosphere (*e.g.* Noyes, Beckers, and Low, 1968; Newstead, 1969; Buhl and Tlamicha, 1970; Kundu, 1970; Lindsey and Hudson, 1976; Labrum, 1978; Kaufmann *et al.*, 1982; Righini and Simon, 1976; Urpo, Krüger, and Hildebrandt, 1986; Kosugi, Ishiguro, and Shibasaki, 1986; Clark *et al.*, 1992; Vršnak *et al.*, 1992; Bastian, Ewell, and Zirin, 1993; Brajša *et al.*, 2007). Millimeter wavelengths probe down into the chromosphere of the Sun where the radiation is optically thick, in contrast to longer radio wavelengths that tend to be dominated by bright coronal sources (*e.g.* White, 1999). Radio emission at millimeter wavelengths is in the Rayleigh-Jeans limit, such that the measured radio brightness temperature is the actual electron temperature in the radiating layer when optically thick, and this makes such observations an important aspect of understanding the temperature structure of the solar atmosphere (*e.g.* Vernazza, Avrett, and Loeser, 1976; Wedemeyer *et al.*, 2016).

Single-dish observations of the Sun have been somewhat neglected in recent years (see however Iwai and Shimojo, 2015) because they have not kept up with the improved spatial resolution available at non-radio wavelengths and with radio–interferometer data: the spatial resolution of single-dish observations is fixed by the aperture of the dish and the wavelength. In addition, the traditional (at least prior to the last decade) single-dish mapping method consisting of dwells at a raster of grid points is a slow technique, particularly with large-aperture dishes constrained by their weight to move slowly, and it is thus poorly suited to tracking the dynamic phenomena typical of the solar chromosphere.

However, with the opening of solar observations by the Atacama Large Millimeter-submillimeter Array (ALMA: Wootten and Thompson, 2009), single-dish data are expected again to be an important feature of studies of the solar chromosphere (Phillips *et al.*, 2015). ALMA will provide superb high-spatial-resolution images of the chromosphere with its large interferometric array operating at wavelengths from 3 to 0.3 mm (see Shimojo *et al.*, 2017). However, the field of view of the interferometric observations is relatively small, and the interferometer is unable to measure spatial scales larger than the fringe spacing corresponding to the shortest baseline in the array, making it insensitive to the absolute temperature of the solar atmosphere. The

absolute temperature scale, and temperature variation with frequency corresponding to different heights in the chromosphere, is crucial for a wide range of ALMA solar science (*e.g.* Wedemeyer *et al.*, 2016). Single-dish data can restore information on the absolute temperature scale missing from the interferometer data. For mapping of larger areas in which the interferometer carries out a mosaic (multiple pointings), the single-dish image will be used to fill in the large spatial scales during deconvolution (*e.g.* Ekers and Rots, 1979; Koda *et al.*, 2009). Two other developments make this technique attractive: in recent years the mapping method for single-dish data has changed to exploit continuous movement of the dish (the so-called "on-the-fly" technique; Mangum, Emerson, and Greisen, 2007), making it much faster; and ALMA incorporates 12 m dishes specifically designed with the ability to scan rapidly yet precisely in order to exploit this technique. A major advantage of these observations is the speed with which the Sun can be mapped, which both permits the study of time-varying phenomena and minimizes the impact of variation in terrestrial atmospheric transmission, which is a major issue for short-wavelength millimeter observations.[1]

It is planned that ALMA interferometer observations of the Sun will be complemented by single-dish (SD) data from several 12 m antennas, permitting redundancy in case of failures at one or more of the antennas. Initially, ALMA solar single-dish mapping will be monomode: full-disk total-power observations with fixed parameters will be carried out continuously at the interferometer observing frequencies. During a solar commissioning campaign in December 2015, tests were carried out in order to have a basis for recommending the SD observing conditions for full science observations of the Sun. These started in late 2016 in Bands 3 (84 – 116 GHz) and 6 (211 – 275 GHz). This article describes the results of the tests, the properties of the SD data, its calibration, and it discusses initial results on the temperatures of the layers that ALMA will probe.

2. Fast-Scan Imaging With ALMA 12 m Dishes

ALMA fast-scan solar imaging will primarily be carried out with four 12 m dishes constructed by the Mitsubishi Electric Corporation (MELCO: Iguchi *et al.*, 2009; Sugimoto *et al.*, 2009) and labelled PM01-PM04.[2] In order to optimize the ability of the dishes to maintain pointing accurately as they scan, an initial characterization of the individual antenna servo response is carried out by comparing commanded and reported antenna positions under a range of conditions and determining the servo gain. Corrections (usually small) can then be implemented in the drive software (*e.g.* Hills, 2016). During the initial phase of ALMA solar observations, ALMA will offer only full-disk SD observations. This will consist of a circular field of view of diameter 2400″ that will be mapped using a "double-circle" scanning pattern. This provides a region of over 200″ off the solar limb encompassing solar prominences above the limb as well as blank-sky regions for checks on calibration. Since there will be no opportunity during the initial solar observations to change the interferometer pointing location on the timescales of minutes that would be necessary to track, *e.g.* a prominence eruption, this field of view should address all likely science use cases relevant for initial observations, while simultaneously optimizing the cadence of single-dish mapping (which is the cadence at which zero-spacing information is obtained for the interferometer target field of view). These restrictions on SD observing may be relaxed in future observing cycles.

Figure 1 shows the scanning pattern on the sky for a double-circle fast-scanning map, taken from actual data from PM02 during the December 2015 commissioning campaign. Essentially the mapping pattern consists of ("minor") circles with diameter half that of the overall field of view (FOV) whose centers move steadily in a ("major") circle around the center of the field of view at a distance that is one-quarter of the diameter of the field of view. An advantage of this pattern is that the continual circular motion allows a steady velocity to be maintained, whereas other patterns, such as Lissajous, often require sharp turns with higher acceleration. Every minor circle passes through the center of the field of view, which means that this location is oversampled compared to regions halfway out to the edge of the FOV, but has the advantage that fluctuations in terrestrial atmospheric transmission (which can have a major impact on the received

[1] Fast-scanning observing with the ALMA dishes was initially developed by Richard Hills and Neil Phillips, with non-solar observing in mind, during several commissioning campaigns starting in 2010. These efforts are documented in the ALMA Commissioning and Science Verification task CSV-203 and attached sub-tasks; specific solar developments are documented under CSV-3162 (2014 campaign) and CSV-3244 (2015).

[2] The twenty-five 12 m antennas built for ALMA by the AEM Consortium, normally used for interferometer observations, are also direct-drive antennas that perform well as fast-scanning dishes, but they will not be discussed in this article.

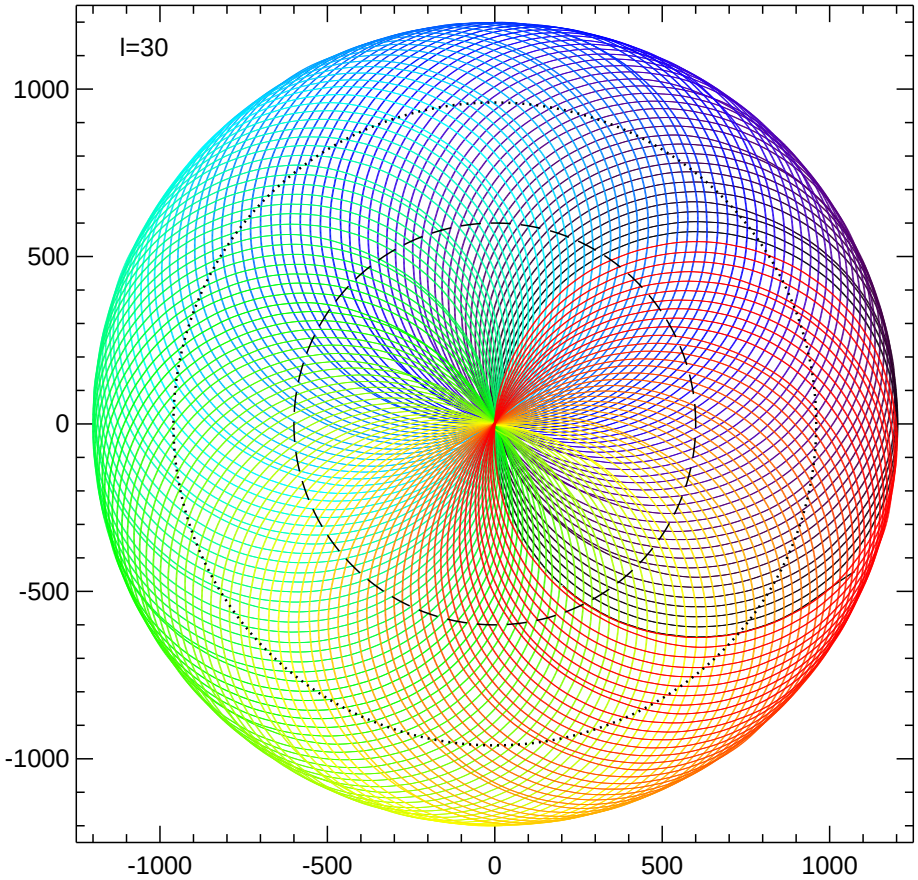

Figure 1. The double-circle pattern for a 2400″ diameter field of view with "map spacing" of 30″. The dashed-line circle at a radius of 600″ is the "major circle" track of the centers of the individual minor circles. The dotted line is the (average) solar limb at a radius of 960″. The color variation of the telescope track is simply a rainbow color table intended to show the progress of the pointing location with time. Mapping started and ended at about the "3 o'clock" location on the figure.

flux and thus produce large artefacts in the resulting maps) can simply be tracked and removed by requiring the central brightness temperature to remain stable. This is not likely to be important for Bands 3 and 6, but it will matter more for later observations at shorter wavelengths where atmospheric opacity is larger.

The SD observing program has a parameter samplingLength [l] which controls the number of minor circles in a pattern by changing the spacing of the centers of the minor circles as they move around the major circle. This parameter needs to be smaller at higher frequencies in order to match the observing pattern to the higher spatial resolution of the dishes. A second parameter, subscanDuration, specifies the duration of on-source mapping, and these two numbers have to be coordinated in order to ensure that a complete map is achieved. In addition, there is no value to having the subscanDuration be significantly longer than required for a full pattern because the additional partial coverage of the solar disk will take extra time without enhancing the resulting image, so the subscanDuration is specified to match the duration of a full pattern.

There are limits to both the permitted maximum acceleration [3° s^{-2}] and velocity [1° s^{-1}] that can safely be used with the PM antennas, and these are taken into account by the control software when converting the desired pointing pattern into the sinusoids to be commanded to the antenna drives, effectively scaling down the frequencies as needed. In the case of the large maps needed for the solar disk, the acceleration limit determines the minor-circle frequency to be about 0.675 Hz and velocity 0.71° s^{-1}. Tests were carried out with the PM antennas to determine the durations of a full pattern for likely values of l, and the results are shown in Table 1.

The results are consistent with a linear relationship between samplingLength and pattern duration resulting from the constant scan rate. The region with the largest spacing (on the sky) between samples is along the major circle. The number of minor circles (each of length 3770″ for a 600″ radius) essentially matches the length of the major circle (also 600″ radius and 3770″ long) divided by the samplingLength parameter. Since

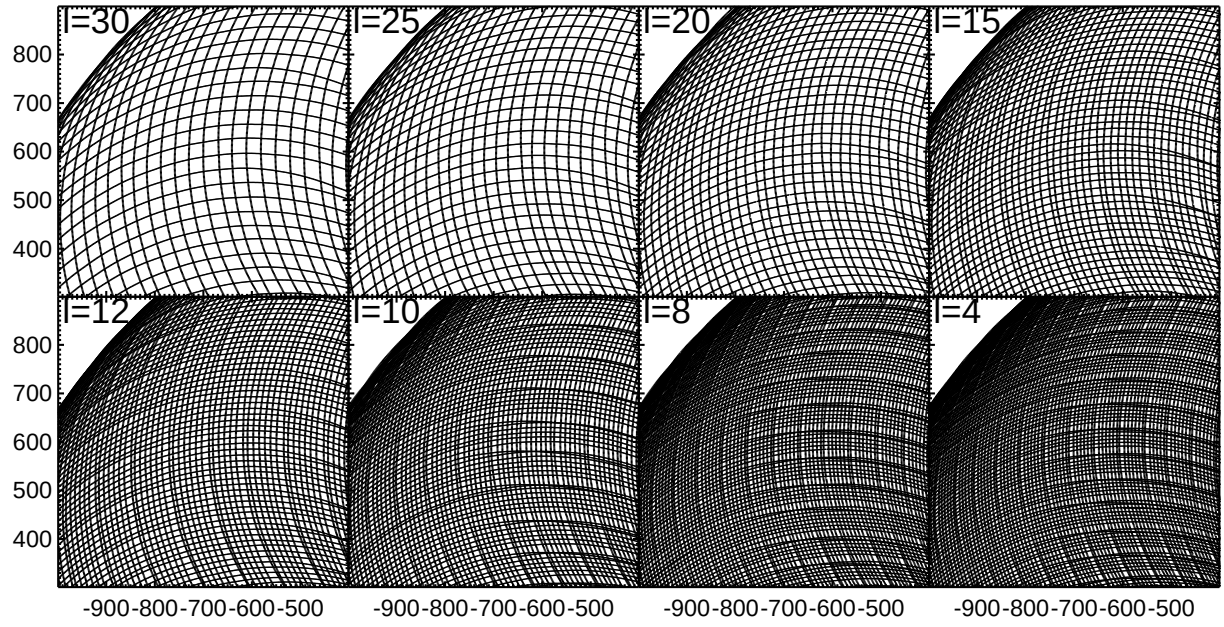

Figure 2. Portions of the fast-scanning patterns for different values of the samplingLength parameter l. Each 1-millisecond sample is plotted as a point, but since the separation of samples along each minor circle is 1.5″, they appear to overlap on the plot. The region plotted is around the major circle at radius 600″ from disk center where we expect the largest holes in the sampling pattern to occur.

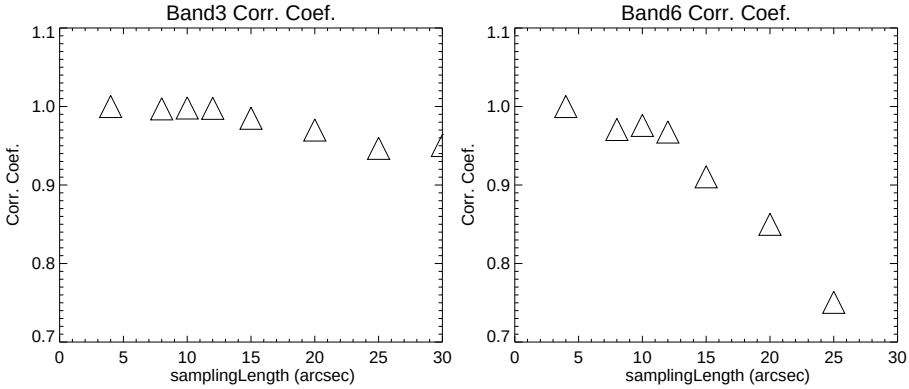

Figure 3. Correlation coefficient of intensity as a function of samplingLength l for Bands 3 and 6, from Iwai (2016a). The plot shows a significant decline for Band 3 at l > 20″ and for Band 6 at l > 12″.

each minor circle crosses the major circle twice, on average the largest distance between sampled points is half the samplingLength parameter, barring unfortunate cases where the minor circle crossings fall on top of each other. In practice, the double-circle pattern seen in fast-scanning observations is not exactly regular. This can be seen by careful inspection of Figure 1, and Figure 2 shows more detail for each of the eight l-values listed in Table 1. Irregularities in the tracks are clearly visible in all patterns, presumably due to imperfections in the servo responses, but the scale of the irregularities in the patterns is not large enough to prevent successful mapping (which grids the sampled points on the sky according to the actual measured pointing locations returned by encoders on each antenna).

Presently there is significant overhead (of order nine minutes) for each single-dish map: both focus and pointing adjustments are first carried out using a very bright source such as a large planet, and atmospheric calibration scans are carried out before and after the solar data acquisition. The nominal spatial resolution of a single dish (with the beam response tapered by 10 dB at the edges to minimize the effects of rear spillover, which is a common design practice for such telescopes) is $1.13\lambda/D$ (full width at half maximum, or FWHM), where λ is the observing wavelength and D is the dish diameter. For the 12 m PM antennas, this corresponds to 58″ at 100 GHz in Band 3 and 25″ at 230 GHz in Band 6. The choice of optimal samplingLength is a trade-off between adequate sampling of the image plane and the additional time required for finer sampling.

Table 1. Pattern durations as a function of samplingLength for a 2400″-diameter circular field-of-view.

samplingLength [arcsec]	Pattern duration [seconds]	Minor circles per pattern
30	187	125
25	224	150
20	280	188
15	373	251
12	467	314
10	560	377
8	701	471
4	1397	943

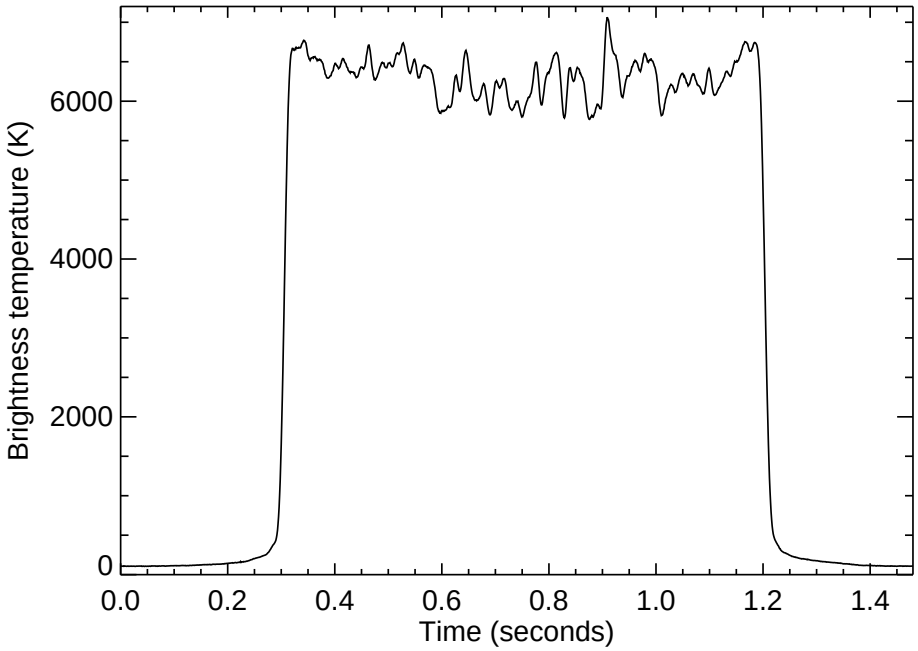

Figure 4. The TP amplitude variation around a single circle of the double-circle pattern. The plot consists of 1480 individual one-millisecond TP measurements at 230 GHz, calibrated to brightness temperature. The 600″ radius circle starts off the limb at 1200″ from disk center and passes onto the limb: from the low level of fluctuations at off-limb positions it is clear that the noise level is insignificant in the one-millisecond integrations and the Sun's signal dominates each sample. All of the temporal variations seen on the disk represent the telescope sweeping over real structures in the solar atmosphere.

Nyquist sampling of the single dish images requires sampling distances of at most 30″ in Band 3 and 12″ in Band 6. Iwai (2016a) has investigated the effect of l on image quality. He took a model solar image, convolved it with the telescope response, sampled it per the fast-scanning patterns shown above with a range of values of l and then imaged the result using a standard triangulation gridding method. He then took a torus just inside the solar limb and determined correlation coefficients against the most densely sampled pattern (l = 4″) as a function of l, with the assumption that sampling with l much smaller than the primary beam provides an appropriate reference curve (unity correlation). The results are shown in Figure 3. The plot shows a significant decline in the correlation coefficients beyond l = 20″ for Band 3 and l = 12″ for Band 6. Based on these results, the fast-scan SD mapping currently uses samplingLengths of l= 20″ for Band 3 (total duration of 13 minutes per full-disk execution including the calibrations described above) and l= 10″ for Band 6 (17 minutes per execution). These parameters achieve Nyquist sampling in the solar disk images.

3. Sampling Time

In addition to the spatial sampling of the scanning pattern embedded in the samplingLength parameter, the quality of the resulting image depends on the interval between data samples. The data being used for SD mapping come from the total power (TP) detectors for each of the four 2 GHz-wide basebands (equivalent to spectral windows for our purposes) provided by the two-stage heterodyne conversion employed by ALMA (described further by Shimojo *et al.*, 2017). These are simple square-law detectors with a hardware sampling time of 0.5 milliseconds. Test fast-scanning observations have generally been carried out with TP data recording times of one or two milliseconds: the Sun is so bright that a one-millisecond sample on the disk is dominated by the solar signal. This is demonstrated in Figure 4, which shows 1480 raw one-millisecond power measurements for a single minor circle of the double-circle pattern, passing onto and then off the solar disk. The temporal variation seen in this figure is due to real structure along the path of the antenna across the solar disk: the noise level for a system temperature of order 1000 K (see below) with 2 GHz bandwidth in 0.5 milliseconds is of order 1 K, *i.e.* $< 10^{-3}$ of the received power in each IF band and polarization, and small compared to the point-to-point variations in amplitude.

For a 2400″ double-circle pattern the average velocity of the telescope of 0.7° s^{-1} (independent of the samplingLength parameter) results in a spatial sampling rate of about 2.5″ on the sky for a TP sampling time of one millisecond. Each minor circle takes about 1.5 seconds (*i.e.* the telescope field of view passes through the disk center region every 1.5 seconds). Such a fine spatial sampling along the path is not required for Nyquist sampling in Bands 3 and 6, but short integrations are valuable for providing flexibility in removing any bad measurements. For the current solar SD observations in Bands 3 and 6, the TP sampling time is one millisecond.

The telescope-pointing information coming from the drive software is not sampled on the same timescale: it has a fixed 48-millisecond interval. During calibration, the ALMA mapping software has to interpolate the pointing data onto the one-millisecond timescale of the total-power samples. The interpolation is not linear, since the telescope path on the sky is curved, so several pointing measurements must be used to get the correct path.

The resulting single-dish files are small by ALMA interferometer standards, but still of significant size: a Band 3 dataset in standard ALMA format with a samplingLength of 20″ and four antennas is 292 MB. For Band 6, a file with samplingLength of 10″ and four antennas is 532 MB.

4. Gridding of Fast-Scan Data

In addition to the dish aperture and tapering of the antenna response to minimize spill-over, the effective spatial resolution of an on-the-fly single-dish image depends on the manner in which the data samples are gridded into an image: the data are smoothed at the irregularly-spaced coordinates corresponding to the pointing locations of the dish when each sample was acquired, and then they are interpolated onto a regular grid. The process of interpolation effectively acts as a convolution, and Mangum, Emerson, and Greisen (2007) discuss this process and the range of functions typically used. The two gridding functions commonly employed in ALMA single-dish imaging are a spheroidal function ("SF") and a "GJinc" function (Gaussian multiplied by a Bessel function). These are implemented in the single-dish mapping tasks in the software package *Common Astronomy Software Applications* (CASA, see casa.nrao.edu) that provides the standard analysis path for ALMA data. CASA also provides tasks to carry out amplitude calibration, discussed further below. CASA scripts for the end-to-end processing of ALMA single-dish fast-scan data are provided with the solar Science Verification data release (see almascience.nrao.edu/alma-data/science-verification).

Brogan and Hunter (2014) have analyzed the effect of different gridding choices on ALMA single-dish data and recommend SF gridding as the standard method for ALMA mapping, while the GJinc function may give slightly better spatial resolution. We note that processed images may still show trace artefacts of the original double-circle scanning pattern, particularly at the limb. Small errors in the assumed pointing of the dish (or small errors in the assumed timing of the samples, which has the same effect) can have a large effect at the limb because the large temperature difference between the cold sky and hot solar disk magnifies the error when the actual relative proportions of those two contributions to the measured power do not match the proportions appropriate to the assumed pointing.

5. Elevation Limitations

The ALMA antennas have azimuth-elevation mounts, which means that at high elevations the azimuth drives must scan much faster than at low elevations for the same distance moved on the sky. Because fast scanning is already driving the antennas at close to the upper limits of their slewing rates, it cannot be carried out at high elevations[3]: empirically, the solar fast-scan patterns described here have been found to be usable up to a maximum elevation of 70°, corresponding to an azimuth acceleration of up to 8.8 deg s^{-2}. The slew rates required for tracking a single point on the solar surface are much less demanding, and interferometric observing is permitted to higher elevations (typically recommended up to about 82°), limited by the potential of azimuth slew durations to and from the phase calibrator becoming excessive, and the risk of either the science target or phase calibrator entering a small zenith avoidance zone that will cause the observation to abort. There is also a lower limit to the elevation of solar interferometric observations of about 40°, imposed by mutual shadowing at lower elevations of the 7 m dishes in the compact array. The implications of the elevation limit on single-dish mapping depend on the time of year that solar observations take place. Since ALMA is at a latitude of 23° south, the Sun passes directly overhead at local noon at the December solstice, and the upper elevation limit means that fast-scan observing is not permitted for a three-hour period centered on local noon. At other times of the year when the Sun does not reach such high elevations, the blocked period will be shorter, but it should be recognized that this restriction on the SD mapping can have an impact on the scheduling of solar programs.

6. Receiver Set-Up

As described by Shimojo *et al.* (2017), observations of the bright solar flux with ALMA require special conditions to achieve a linear response in the sensitive receivers. Originally it was planned that special solar attenuators would be placed in the beam path to reduce the signal reaching the receivers, but this approach has a number of disadvantages: notably the amount of attenuation is fixed, and the attenuators will impose complex gain variations on the signals that would need careful and extensive measurements at every observing frequency on every antenna for correction. Furthermore, since the solar attenuators are located in the same filter-wheel as the calibration loads, standard ALMA calibration cannot be carried out through the solar attenuators. Subsequently, Yagoubov (2013) described a detuning technique in which the ALMA Superconductor-Insulator-Superconductor (SIS) mixer voltages are not biassed to their usual, and highest gain, values near the middle of the first photon step below the superconducting gap voltage, but to other photon steps above or below the gap voltage that have lower gain. In addition, the local oscillator power supplied to the SIS mixers can be used to fine-tune the resulting gain. These alternate "solar tuning" mixer-bias voltages have been determined for the ALMA receivers in Bands 3 and 6 (see further discussion in Shimojo *et al.*, 2017). For single–dish solar observations, data will be taken with the "MD2" bias, *i.e.* the second photon step above the superconducting gap voltage for Band 3 and the first photon step above the gap for Band 6, resulting in system temperatures of order 1000 K in both bands, rather than the values of order 40 K resulting from normal bias: the lower gain of the MD2 bias provides linearity for the wide range of solar brightness temperatures (up to 8000 K) given the dynamic range of the ALMA system. The receivers are believed to respond linearly in this temperature range, although we cannot rule out the possibility that there is a small amount of gain compression (a few percent: see Iwai, 2016b); the linearity of the receivers with the MD2 bias at the much higher antenna temperatures that may occur during solar flares has not yet been investigated.

The observing frequencies used for single-dish mapping will be fixed to match the interferometer observations (see Shimojo *et al.*, 2017): there will be four continuum basebands, each 2 GHz wide. The frequencies are shown in Table 2. The single-dish mapping will initially measure continuum emission only and will be carried out using the total power detectors associated with each baseband in both linear polarizations (X and Y) simultaneously, providing eight different data streams. In the future, spectral-line capability will be available for solar observations: at present, single-dish spectral-line observations require the use of a correlator.

[3]The solar team can confirm that trying to observe at higher elevations does drive the antennas into a non-functioning state: the prolonged excessive accelerations can cause the drive power amplifiers of the PM antennas to trigger an over-current cut-out, requiring manual reset by a human at the antenna to recover operation.

Table 2. Continuum frequencies for ALMA Cyle 4 solar observations. These are the central frequencies of the 2-GHz-wide basebands.

	BB 1 GHz	BB 2 GHz	BB 3 GHz	BB 4 GHz
Band 3	93.0	95.0	105.0	107.0
Band 6	230.0	232.0	246.0	248.0

7. Calibration Measurements

Since we are using the ALMA single-dish data to supply the background brightness temperature scale that the interferometer data cannot measure, calibration is a very important aspect of the solar fast-scanning observations. A standard calibration technique is to use observations of a reference source of known flux to scale the data: this technique is difficult for the solar observations due to the high system temperature and the lack of bright sources other than the Moon that fill the beam as the Sun does. Instead, we use an approach developed for single-dish data, modified for our observing technique. Calibration relies on measurements made with the ALMA Calibration Device (Casalta *et al.*, 2008; Yagoubov *et al.*, 2011; van Kempen *et al.*, 2012) located in each antenna: this system is capable of placing two microwave absorbers at different temperatures, the "ambient" (nominally 20° C) and "hot" (nominally 85° C) loads, in front of the receiver feed horns of any of the bands. At the beginning and end of the SD observation, five-second measurements of the receiver signal level are made for the following targets:

- a "sky" observation offset (by typically 2°) from and at the same elevation as the target;
- an "ambient" load observation that fills the beam path at the temperature of the thermally-controlled receiver cabin (nominally 20° C);
- a "hot" load observation that fills the beam path;
- a "zero" level measurement, which reports the power levels in the detectors when no signal power is being supplied. In the case of ALMA, the zero levels are very stable over many days for a given antenna and receiver;
- and finally, a second measurement of the power level on the sky, called the "off" level, made after the telescope has moved to the target (in our case, the Sun) where the intermediate-frequency-stage (IF) attenuation levels are reset to values appropriate for the power being seen. Since the Sun is much brighter than other sources, the increased attenuation results in a lower power than the first sky measurement.

The fact that two different intermediate-frequency-stage attenuation settings are required means that, unlike normal single-dish observations, two different receiver gains must be solved for.

Since the sky is being used as a calibration source, we need to know its effective temperature contribution, which requires knowledge of the atmospheric temperature and the opacity of the atmosphere. These are measured by a separate device, the water vapor radiometer (WVR), attached to each antenna (Hills, 2010; Nikolic *et al.*, 2013). This device measures the shape and intensity of the water vapor line at 183 GHz, and in combination with an atmospheric model (in the case of ALMA, the ATM model: Pardo, Cernicharo, and Serabyn, 2001) provides the precipitable water vapor (PWV) level that is an important opacity source at millimeter wavelengths. The atmospheric model also includes the contributions of other atmospheric species.

8. Calibration Analysis

We label the median powers from the calibration scans as $P_{\rm sky}$, $P_{\rm amb}$, $P_{\rm hot}$, $P_{\rm zero}$, and $P_{\rm off}$ for sky, ambient, hot, zero, and off, respectively; T denotes the corresponding temperatures. The standard method for calibrating millimeter data is to determine the system temperature [$T_{\rm sys}$], *i.e.* the total thermal noise level in the system excluding the target source, and then apply it to the power measurements according to some form of the algorithm

$$T_{\rm src} \;=\; T_{\rm sys}\;\frac{P_{\rm src}\;-\;P_{\rm ref}}{P_{\rm ref}} \tag{1}$$

(*e.g.* Ulich and Haas, 1976; Kutner and Ulich, 1981; Mangum, 1993) where $P_{\rm src}$ is the power measured while pointing at the target source, and $P_{\rm ref}$ is the power measured at a reference position that corresponds to the $T_{\rm sys}$ measurement (*i.e.* no source power). Calibration by this method amounts to determining $T_{\rm sys}$.

8.1. Dual-Load Calibration

An approach that uses both loads in the ALMA Calibration System is as follows. The power measured by a sky observation can be expressed as

$$P_{\rm sky} \;=\; G\{T_{\rm rec}\;+\;(1-{\rm e}^{-\tau})\eta_{\rm l}T_{\rm atm}\;+\;(1\;-\;\eta_{\rm l})\,T_{\rm spill}\;+\;{\rm e}^{-\tau}\eta_{\rm l}T_{\rm CMB}\}\;+\;P_{\rm zero} \tag{2}$$

where G is the gain; $T_{\rm rec}$ is the intrinsic thermal noise of the receiver; $\eta_{\rm l}$ is the antenna efficiency for a source that is much larger than the primary beam; $T_{\rm atm}$ is the temperature of the (optically thin) layer of the atmosphere that dominates the optical depth; and τ is the opacity of the atmosphere (for a given telescope elevation El, τ is the zenith opacity τ_0 times the "air mass" $1/\sin(El)$). $\eta_{\rm l}$ is referred to as the *forward efficiency* (Tamura and Sugimoto, 2012), and it is the product of the efficiency $\eta_{\rm r}$ that accounts for ohmic losses (heating of the dish surface by the incident radiation) and the efficiency $\eta_{\rm rss}$, the *rear spillover efficiency*, that accounts for signal not reflected from the main dish (*e.g.* ground illuminated beyond the edge of the dish) that reflects off the subreflector or other surface above the dish and enters the receiver. The effective temperature of this contribution [$T_{\rm spill}$] is usually at the ambient temperature of the telescope.

Above the atmosphere, the sky is filled by the cosmic microwave background (CMB). The combination ${\rm e}^{-\tau}T_{\rm CMB} + (1-{\rm e}^{-\tau})T_{\rm atm}$ in Equation (2) is the result of radiative transfer of the sky background temperature $T_{\rm CMB}$ through a layer with optical depth τ and temperature $T_{\rm atm}$. Although we use simple temperatures in the formulae presented here, in each case the relevant value to use is the equivalent Rayleigh-Jeans radiation temperature at the point on the black-body curve corresponding to the observing frequency ν, $J(\nu,T) \;=\; (h\nu/k_{\rm B})/(\exp(h\nu/k_{\rm B}T)-1)$, where h is Planck's constant and $k_{\rm B}$ is Boltzmann's constant. For example, the temperature of the CMB is 2.73 K, but the temperature we need at millimeter wavelengths [$T_{\rm CMB}$] is the Rayleigh-Jeans curve equivalent $J(\nu, 2.73) \approx 1$ K at 3 mm wavelength. In the 3 mm window $J(T) \approx T - 2.4$ to quite a good approximation above a few tens of K, and $J(T) \approx T - 5.5$ in the 1.3 mm window, so the difference between T and $J(T)$ is negligible for our purposes.

When the ambient and hot loads are placed in front of the receiver, they fill the optical path. The received powers are

$$P_{\rm amb} \;=\; G\{T_{\rm rec}\;+\;T_{\rm amb}\}\;+\;P_{\rm zero} \tag{3}$$

and

$$P_{\rm hot} \;=\; G\{T_{\rm rec}\;+\;T_{\rm hot}\}\;+\;P_{\rm zero}. \tag{4}$$

The power on the target source is

$$P_{\rm src} \;=\; G_{\rm src}\{T_{\rm rec}\;+\;{\rm e}^{-\tau}\eta_{\rm l}\,T^{*}_{\rm src}\;+\;(1-{\rm e}^{-\tau})\eta_{\rm l}T_{\rm atm}\;+\;(1\;-\;\eta_{\rm l})\,T_{\rm spill}\}\;+\;P_{\rm zero} \tag{5}$$

where the gain [$G_{\rm src}$] is different from G due to the different IF attenuation setting used for the Sun. $T^{*}_{\rm src}$ is the source brightness temperature. In the case of a source much larger than the telescope beam, such as the Sun or the Moon, the target replaces the CMB as the background temperature. The power measured at the "off" position on the sky with the same attenuation as the source measurement is, by analogy with Equation (2),

$$P_{\rm off} \;=\; G_{\rm src}\{T_{\rm rec}\;+\;(1-{\rm e}^{-\tau})\eta_{\rm l}T_{\rm atm}\;+\;(1\;-\;\eta_{\rm l})\,T_{\rm spill}\;+\;{\rm e}^{-\tau}\eta_{\rm l}T_{\rm CMB}\}\;+\;P_{\rm zero} \tag{6}$$

We can now solve these equations for $T^{*}_{\rm src}$. The gain G is derived from Equations (3) and (4) as

$$G \;=\; \frac{P_{\rm hot} \,-\, P_{\rm amb}}{T_{\rm hot} \,-\, T_{\rm amb}} \tag{7}$$

where typically $T_{\rm amb} = 291^\circ$ K and $T_{\rm hot} = 357^\circ$ K. We can derive the source gain simply from the ratio of Equation (6) to Equation (2),

$$G_{\rm src} \;=\; G\,\frac{P_{\rm off} \,-\, P_{\rm zero}}{P_{\rm sky} \,-\, P_{\rm zero}} \tag{8}$$

Note that when observing the Sun in MD2 mode with large system temperature, $P_{\rm zero}$ is generally much smaller than the other calibration measurements, but with normal mixer bias the IF attenuation is set to much higher values to ensure acceptable power levels from the Sun, and then $P_{\rm off}$, also measured with the higher attenuation, becomes much smaller and can be of the same order as $P_{\rm zero}$. In that case neglecting $P_{\rm zero}$ leads to major errors. Even with MD2 bias, as we show below, neglect of $P_{\rm zero}$ can lead to errors of over 10 % which are larger than we want for solar calibration. Note that $P_{\rm zero}$ is only relevant for data from the total-power square-law detectors, not for correlation data.

The receiver temperature is determined from Equations (3) and (7) to be

$$T_{\rm rec} \;=\; \frac{T_{\rm hot}\,(P_{\rm amb} \,-\, P_{\rm zero}) \,-\, T_{\rm amb}\,(P_{\rm hot} \,-\, P_{\rm zero})}{P_{\rm hot} \,-\, P_{\rm amb}} \tag{9}$$

$T_{\rm atm}$ and τ are provided by the standard ALMA calibration method as described above. In any case, we have sufficient measurements to determine the sky contribution without using the atmospheric data from the WVR: using Equations (2) and (7), we find, setting $P_{\rm sky} - P_{\rm zero} = G(T_{\rm rec} + T_{\rm sky})$, that the "sky" temperature contribution (including rear spillover, which is actually not from the sky) is of the form

$$T_{\rm sky} \;=\; (1-{\rm e}^{-\tau})\eta_{\rm l}\,T_{\rm atm} \,+\, {\rm e}^{-\tau}\eta_{\rm l}T_{\rm CMB} \,+\, (1 \,-\, \eta_{\rm l})\,T_{\rm spill} \;=\; \frac{P_{\rm sky} \,-\, P_{\rm zero}}{G} \,-\, T_{\rm rec} \tag{10}$$

where all quantities on the right result from calibration power measurements. Note that conventionally the system temperature (at the telescope, not above the atmosphere) is $T_{\rm sys} = T_{\rm rec} + T_{\rm sky}$. We now subtract Equation (6) from Equation (5) (ignoring the CMB contribution of less than 1 K compared to the ≈1000 K system temperature) and apply Equations (7) and (8) to find

$$T^*_{\rm src} \;=\; \frac{P_{\rm sky} \,-\, P_{\rm zero}}{P_{\rm off} \,-\, P_{\rm zero}}\;\frac{P_{\rm src} \,-\, P_{\rm off}}{P_{\rm hot} \,-\, P_{\rm amb}}\;\frac{T_{\rm hot} \,-\, T_{\rm amb}}{\eta_{\rm l}\,{\rm e}^{-\tau}} \tag{11}$$

As will be shown below, $P_{\rm off}$ is always smaller than $P_{\rm sky}$ in the solar observations due to the larger IF attenuation. By analogy with Equation (1), our expression for the system temperature that can be compared with values calculated by the ALMA on-line calibration system is

$$T_{\rm sys} \;=\; \frac{P_{\rm sky} \,-\, P_{\rm zero}}{P_{\rm hot} \,-\, P_{\rm amb}}\;\frac{T_{\rm hot} \,-\, T_{\rm amb}}{\eta_{\rm l}\,{\rm e}^{-\tau}} \tag{12}$$

where we correct for the atmosphere and forward efficiency since those corrections are applied to the $T_{\rm sys}$ values stored in ALMA datasets.

8.2. Atmospheric Opacities

As described earlier, ALMA uses measurements of the 183 GHz water-vapor line together with an atmospheric model to infer the atmospheric opacity and effective temperature required in the expressions above. The results of fitting the 183 GHz water line by the WVR are supplied to the atmospheric model, which is then used to calculate opacities at the frequencies of each of the basebands being observed, so there are generally four values of τ provided with each dataset. At present, provision of these data for analysis requires connection of an antenna to an ALMA correlator, and hence the WVR data from the individual PM antennas are not available during solar observations since they are only using their total-power detectors and are not connected to a correlator. In this case, the ALMA on-line system seeks a default water-vapor

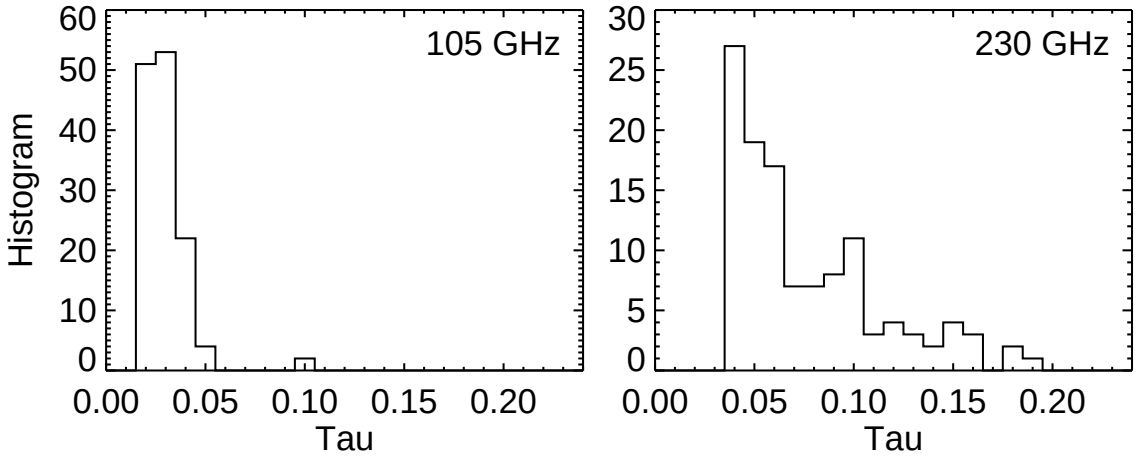

Figure 5. The distributions of daytime atmospheric opacity τ at Bands 3 (105 GHz, left panel) and 6 (230 GHz, right panel) extracted from solar single-dish datasets in 2015 and 2016.

measurement to use, usually from the nearest 12 m antenna that is connected to a correlator (as all the antennas in the interferometric array are). The PM antennas are often located on pads close to the fixed array of 7 m antennas, and frequently seem to be provided with identical sets of opacities. Figure 5 shows the typical range of daytime opacities measured at ALMA (at the source elevation, not the zenith values) for one baseband in each of Bands 3 and 6: at Band 3 τ is reliably below 0.05, whereas at Band 6 the smallest value is around 0.04 and the normal spread reaches up to at least 0.15. In practice ALMA science operations take τ into account when deciding what projects to run, so at the higher values seen at Band 6 in Figure 5, Band 6 projects would probably not be run.

8.3. ALMA System Calibration

As described above, ALMA carries out a set of atmospheric-calibration measurements at the beginning and end of each fast-scanning single-dish dataset. These measurements are used by the ALMA TELCAL software component (Broguière *et al.*, 2011) to calculate the system temperature and atmospheric opacity in real time, and those measurements are passed on in the data to be used in the production of the final calibrated map. The calibration measurements can be extracted from the data files using tools within CASA.

ALMA's system-temperature calculation employs the "improved dual-load" method described by Lucas (2012) and presented in the ALMA Technical Handbook (*e.g.* section A.5.1 in Warmels and Remijan, 2017), in which a combination of the ambient and hot loads is used to approximate a load that matches the temperature of the atmosphere. In practice we find that the system temperatures calculated by TELCAL and reported by CASA are generally within ± 5 % of the single-load calculation,

$$T_{\rm sys} \;=\; \frac{P_{\rm sky} \,-\, P_{\rm zero}}{P_{\rm amb} \,-\, P_{\rm sky}} \, \frac{T_{\rm amb}}{\eta_{\rm l}\, {\rm e}^{-\tau}} \tag{13}$$

(discussed further below in reference to Table 4). The scaling factor $g \,=\, T_{\rm sys}/P_{\rm ref}$ from Equation (1) needed to convert the target power to a temperature measurement is then

$$g \;=\; \frac{T_{\rm sys}}{P_{\rm off} \,-\, P_{\rm zero}} \tag{14}$$

so that the single-load expression for calibration is

$$T^{*}_{\rm src} \;=\; \frac{P_{\rm sky} \,-\, P_{\rm zero}}{P_{\rm off} \,-\, P_{\rm zero}} \, \frac{P_{\rm src} \,-\, P_{\rm off}}{P_{\rm amb} \,-\, P_{\rm sky}} \, \frac{T_{\rm amb}}{\eta_{\rm l}\, {\rm e}^{-\tau}} \tag{15}$$

8.4. Absolute Brightness Temperatures

The result for $T^*_{\rm src}$ in (11) is not the final result that we need for the measurement of solar atmospheric temperatures. A plethora of temperature scales exists in the literature of millimeter-wave astronomy (*e.g.* Jewell, 2002; Mangum, 2002), and $T^*_{\rm src}$ is the source temperature on the telescope-dependent "T^*_A" scale in which the antenna temperature is corrected for atmospheric attenuation, radiative loss, and rearward scattering and spillover (Kutner and Ulich, 1981; Mangum, 1993), but it does not account for signal that enters the receiver from outside the subreflector, usually due to the receiver pattern "seeing" beyond the edge of the subreflector. The corresponding efficiency [$\eta_{\rm fss}$] is called the "forward scattering and spillover" efficiency, and the resulting contribution [$1 - \eta_{\rm fss}$] is therefore usually at the temperature of the sky at the target elevation.

To derive the actual brightness temperature of the Sun [$T_{\rm src}$] that would be seen by a perfect telescope above the atmosphere, we need to divide $T^*_{\rm src}$ by $\eta_{\rm fss}$ (*e.g.* Jewell, 2002), so that

$$T_{\rm src} \;=\; \frac{P_{\rm sky} - P_{\rm zero}}{P_{\rm off} - P_{\rm zero}} \, \frac{P_{\rm src} - P_{\rm off}}{P_{\rm hot} - P_{\rm amb}} \, \frac{T_{\rm hot} - T_{\rm amb}}{\eta_{\rm l}\, \eta_{\rm fss}\, {\rm e}^{-\tau}} \tag{16}$$

For an optically thick source such as the solar chromosphere, this brightness temperature should be the actual temperature of the optically thick layer producing the millimeter-wavelength emission.[4] In practice there will also be a contribution to the measured brightness temperature from the optically-thin hot corona lying above the chromosphere, which could be as much as a few hundred K in Band 3 from the densest parts of the corona and scales with the inverse-square of frequency (*e.g.* White, 1999).

Table 3. Antenna efficiencies used for solar calibration. The final column gives the correction factor $0.98/\eta_{\rm l}/\eta_{\rm fss}$ to be applied to solar single-dish images currently produced by standard processing of ALMA data in CASA, which assumes $\eta_{\rm l} = 0.98$ and does not correct for $\eta_{\rm fss}$.

	Forward efficiency [$\eta_{\rm l}$]	Forward scattering and spillover [$\eta_{\rm fss}$]	CASA correction factor
Band 3	0.96 ± 0.02	0.91 ± 0.03	1.12
Band 6	0.95 ± 0.03	0.89 ± 0.03	1.16

8.5. Antenna Efficiencies

Unfortunately, neither $\eta_{\rm l}$ nor $\eta_{\rm fss}$ is well measured for the ALMA dishes. This does not affect calibration of interferometric data since amplitudes are scaled to astronomical calibrators; similarly, single-dish observations carried out with the full sensitivity of normal receiver bias can also usually be scaled to known bright calibrators such as planets. The TELCAL package that determines system temperatures for ALMA observations uses a fixed value $\eta_{\rm l} = 0.98$ for all bands. This is likely to be an overestimate of the true value, and it is unlikely that the same value applies to all bands since different wavelengths can be expected to have different scattering properties for a fixed antenna geometry. Tamura and Sugimoto (2012) used sky-dip measurements, effectively just varying the elevation and hence τ in Equation (2), to carry out measurements of $\eta_{\rm l}$ that included the PM antennas. This is a difficult measurement because the dependence of Equation (2) on $\eta_{\rm l}$ is weak when τ is small, as it usually is for Bands 3 and 6, and any errors in $T_{\rm rec}$ will affect the results. There is considerable variation across the antennas measured. The results are average values for the PM antennas of 0.94 at Band 3 and 0.92 at Band 6, with systematic uncertainties of at least 5 %. These values are smaller than the nominal ALMA System Technical Requirement of $\eta_{\rm l} > 0.95$. Tamura and Sugimoto (2012) note that limiting the data to higher elevation measurements, where all of the rear spillover comes from the ground as assumed, tends to increase the resulting values. Since the TELCAL value of 0.98 is believed to be too large and the measurements of Tamura and Sugimoto (2012) may be slightly low, in the absence of better data we choose to minimize the uncertainty in the value that we apply by using the average of these results and the TELCAL value of 0.98. This produces the values listed in Table 3: the

[4] Technically this measurement is on the "T^*_R" temperature scale (Jewell, 2002), but since the Sun is so much larger than the beam the source-coupling factor can be assumed to be unity and effectively this is the true source brightness temperature.

uncertainties associated with the choice of these values are unfortunate but we have no better measurements at present.

For $\eta_{\rm fss}$ there are two components to be considered. The "forward spillover" results from the receiver being able to see the sky beyond the edges of the subreflector on a Cassegrain telescope. Measurements of forward spillover have been carried out during commissioning and from a table of results provided by P. Yagoubov (private communication 2016), the MELCO antennas have an average spillover value of 0.04 ± 0.01 at Band 3 and 0.06 ± 0.01 at Band 6. In addition, blockage of the dish by the subreflector supports and scattering from the central cone of the subreflector contribute an extra 5 % (Sugimoto *et al.*, 2009, M. Sugimoto and P. Yagoubov, private communication, 2016). Combining these two contributions gives the values for $\eta_{\rm fss}$ reported in the middle column of Table 3. Finally, since currently ALMA calibration assumes $\eta_{\rm l}$=0.98 and the standard single-dish calibration using the $T_{\rm sys}$ values from TELCAL does not correct for $\eta_{\rm fss}$, the single-dish images resulting from standard processing with ALMA calibration in CASA need to be corrected to obtain the true solar brightness temperatures: the final column of Table 3 gives multiplication factors $(0.98/\eta_{\rm l}/\eta_{\rm fss})$ for this correction.[5] Efforts continue at ALMA to provide better measurements of these quantities, which may change the scaling of the data in the future.

An independent means of calibrating the Sun's brightness temperature that avoids the need for detailed knowledge of antenna-beam efficiencies is to use the Moon as a flux standard (*e.g.* Linsky, 1973a,b). The solid angle of the Moon nearly matches that of the Sun and so measurements of the Moon can be compared directly with those of the Sun. Use of the Moon for calibration relies on the accuracy of lunar models for the time-, frequency- and position-varying response of the lunar surface to solar illumination. This undertaking is significant and will be investigated in a future article.

9. Fast-Scanning Solar Data from ALMA

9.1. Calibration Example

CASA does not currently implement the calibration scheme represented by Equation (16). In order to investigate the temperatures produced by this method, we derived all of the data required to implement Equation (16) from the CASA data files using tools to extract table contents. An example of the resulting calibration data, from a Band 6 dataset, is shown in Table 4. The top five rows show the power measurements for each of the five calibration points described earlier, for each baseband and polarization. The values shown are averages of the middle section of each calibration scan, representing about 2500 one-millisecond samples. The standard deviation over this set of samples is 0.1 % or less of the average values for all measurements except $P_{\rm zero}$, so the third digit is significant. Note that the $P_{\rm zero}$ values are mostly small compared to the other calibration data, as expected with the MD2 bias, and the standard deviation of the data used to determine $P_{\rm zero}$ is at the 10^{-4} level on the scale shown in Table 4. However, even with these small values, for polarization Y at 248 GHz (baseband 4) $P_{\rm zero}$ is about 12 % of $P_{\rm off}$, and since $(P_{\rm off} - P_{\rm zero})$ appears in the denominator of (16), neglect of $P_{\rm zero}$ can result in about a 10 % difference in the temperature scale in this case, which would be important for solar studies.

We carry out the calculations for each of the four observed frequencies and each of the two linear polarizations separately: we argue that all eight variants in a dataset should give similar results since solar emission is not linearly polarized and the relatively small frequency differences between the four basebands are not large enough to show up as significant temperature differences in the final results. The fact that the X- and Y-maps should give the same temperature at a given frequency is used by Shimojo *et al.* (2017) to determine the noise level in solar interferometry maps. Table 4 shows the typical level of variation seen in the calibration, resulting in large variations in both the receiver temperature $[T_{\rm rec}]$ and the system temperatures $[T_{\rm sys}]$ across the eight samples. The system temperature from Equation (12) derived using the two loads is often lower than both the single-load system temperature from Equation (13) and the values supplied to CASA by TELCAL following the Lucas (2012) approach. The two latter values are generally similar but not identical to each other. As expected, all values are around 1000 K rather than the values of 40 – 50 K typically found with the normal receiver bias.

[5] Note that in the standard CASA single-dish calibration script this correction is applied as a "gain" in the gencal task. Since gains refer to values for each antenna that are then multiplied together in pairs to correct visibilities between two antennas, in the case of single-dish data the gain supplied is the inverse square-root of the correction factor. Alternatively, the correction factor can be applied directly after the imaging step with the immath task.

Table 4. Calibration measurements from a representative Band 6 dataset using antenna PM04. The first five rows are median power measurements for each of the calibration points described in Section 7, in arbitrary units, for each baseband (four frequencies, as labelled) and linear polarization (X, Y). The τ-measurements are as reported by the on-line system, while the receiver temperature $T_{\rm rec}$ is calculated using Equation (9) and the sky temperature contribution $T_{\rm sky}$ is calculated using Equation (10). The "dual-load" system temperature $T_{\rm sys}^{\rm dual}$ is given by Equation (12), the single (ambient) load system temperature $T_{\rm sys}^{\rm ambient}$ by Equation (13), while $T_{\rm sys}^{\rm Atmcal}$ reports the actual values used by ALMA for calibration, extracted from the data sets. In order to illustrate the results of different calibration methods, the final rows report the median brightness temperature in an $80'' \times 80''$ region centered at apparent disk center for each of the three calibration approaches. $T_{\rm B}^{\rm dual}$ is the result of a direct application of Equation (16), $T_{\rm B}^{\rm ambient}$ results from using the single-load calibration Equation (15) with the correction for $\eta_{\rm fss}$, while $T_{\rm B}^{\rm Atmcal}$ results from processing the data with CASA and then correcting for the chosen values of $\eta_{\rm l}$ and $\eta_{\rm fss}$.

	230 GHz		232 GHz		246 GHz		248 GHz	
	X	Y	X	Y	X	Y	X	Y
Hot	0.629	0.560	0.579	0.565	0.586	0.494	0.593	0.517
Ambient	0.590	0.534	0.545	0.539	0.553	0.472	0.560	0.493
Sky	0.456	0.447	0.426	0.453	0.437	0.402	0.446	0.417
Off	0.257	0.319	0.254	0.317	0.268	0.311	0.267	0.329
Zero	0.002	-0.001	0.009	-0.003	0.007	-0.011	0.007	-0.038
τ	0.142	0.142	0.156	0.156	0.156	0.156	0.182	0.182
$T_{\rm rec}$ [K]	729	1058	754	1092	790	1195	807	1176
$T_{\rm sky}$ [K]	57.8	71.2	60.9	72.1	61.6	74.4	65.3	80.2
$T_{\rm sys}^{\rm dual}$ [K]	955	1370	1003	1432	1048	1562	1101	1585
$T_{\rm sys}^{\rm ambient}$ [K]	1191	1814	1268	1904	1329	2097	1420	2189
$T_{\rm sys}^{\rm Atmcal}$ [K]	1019	1575	996	1478	1041	1621	1159	1826
Disk $T_{\rm B}^{\rm dual}$ [K]	5955	5979	5963	5990	5876	5907	5889	5903
Disk $T_{\rm B}^{\rm ambient}$ [K]	6124	6523	6128	6471	6056	6447	6012	6453
Disk $T_{\rm B}^{\rm Atmcal}$ [K]	6507	7107	5907	6454	5874	6548	6226	7820

Finally, the last three rows of Table 4 compare the brightness temperatures at the apparent center of the solar disk derived using the three calibration schemes. The first set of values is derived by application of Equation (16), the second by application of Equation (15) using the single-load method with correction for efficiencies, while the last row results from processing the data through CASA and applying the correction factor given in Table 3 to the resulting images. The dramatic result of this comparison is that the eight values resulting from application of Equation (16) are very close to each other despite the fact that the corresponding system temperatures have a significant range: the disk center temperatures are consistent to within better than 1 % in this case, even though the system temperatures have a standard deviation of 20 % about their mean. Much of this variation is due to a consistent difference between the two polarizations: in all of the calibration methods the system temperatures of all four sets of Y-polarization measurements are several hundred K larger than those of the X-polarization measurements. This difference shows up strongly in the solar temperatures calibrated with the single-load and the version produced by the standard ALMA path through CASA: the Y-polarization maps give much larger temperatures than the X-polarization maps. Accordingly, the values resulting from standard ALMA calibration appear to be less reliable than those obtained using Equation (16), and work is underway to reconcile these differences.

9.2. Solar Brightness Temperatures

Although chosen at random, the above example of solar data is not necessarily typical of an arbitrary solar dataset. In order to establish the characteristics of solar fast-scanning data, a large number of datasets from 2015 and 2016 have been processed, and it is frequently found that the calibration using Equation (16) does not produce consistent results. The datasets consist of the commissioning data from the December 2015

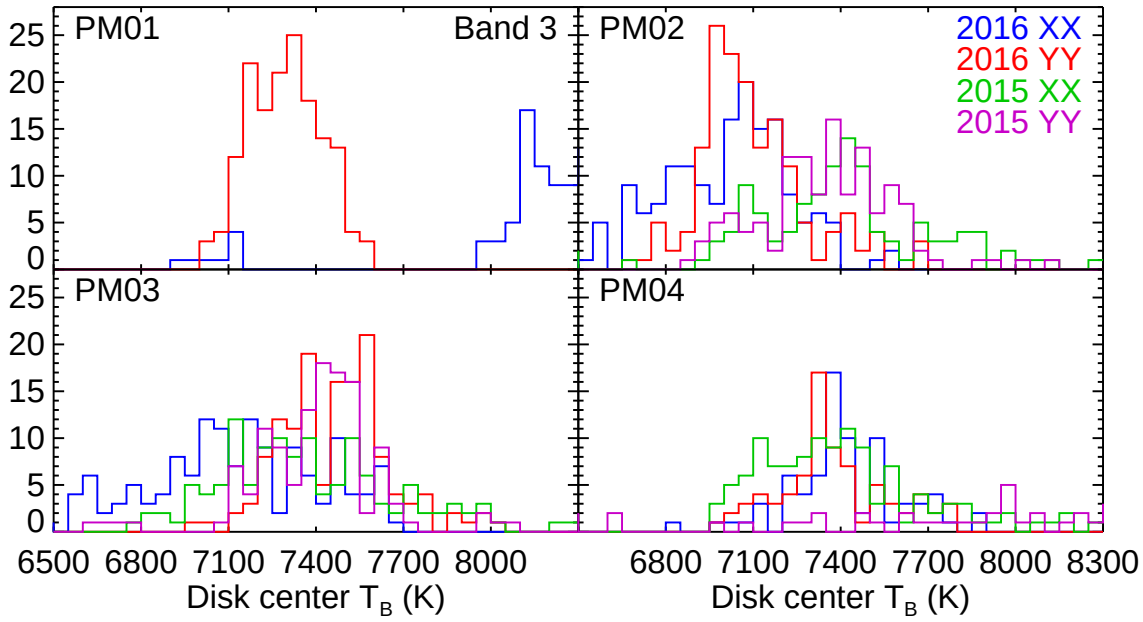

Figure 6. The distributions of the median brightness temperature obtained in a $120'' \times 120''$ region at disk center (beam size $\approx 60''$) for Band 3 datasets from 2015 and 2016. The data are separated by antenna, year, and polarization, as labelled. All four basebands (see Table 2) are included as separate values in the histograms. Note that there were no measurements with PM01 in 2015, and as noted in the text, PM01 and PM03 have poor calibration in polarization Y in 2016, while PM04 is poor at Y in 2015.

campaign and test datasets from the second half of 2016, when solar activity was much lower than during the 2015 campaign. It is found to be common that one polarization gives systematically different results from the other, particularly for a given antenna at a given band. For example, in 2015, PM04 had trouble measuring $P_{\rm zero}$ in polarization Y at Band 3, so those brightness temperatures vary wildly, whereas the X brightness temperatures were much more consistent. In 2016, both PM01 and PM03 produced consistently excessive brightness temperatures in polarization X at Band 3 while the corresponding Y brightness temperatures were more normal.

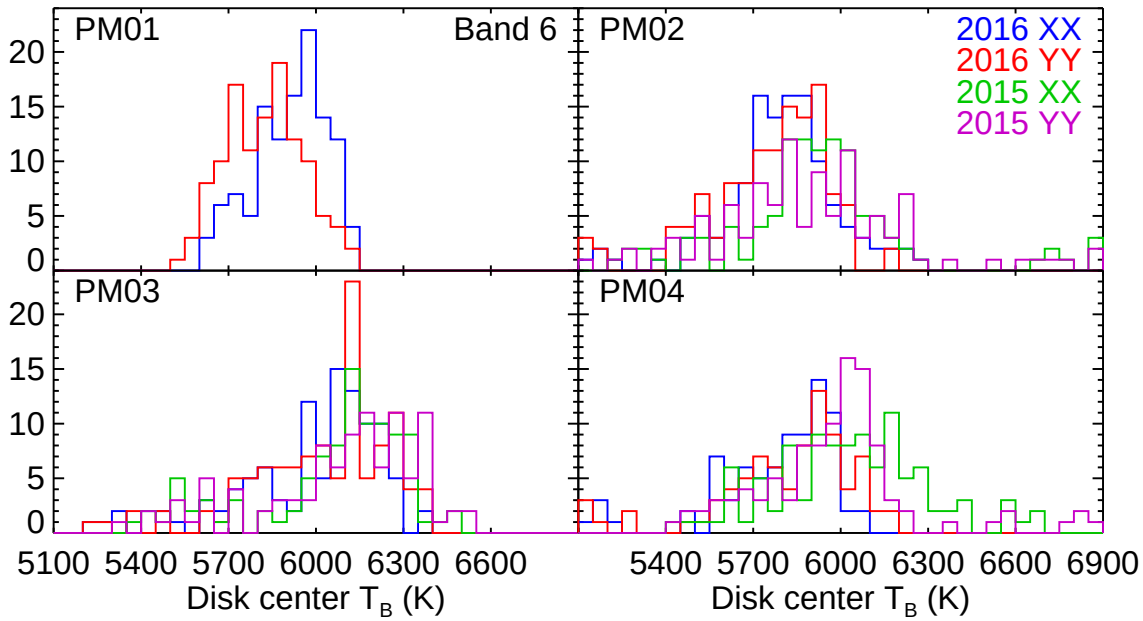

Figure 7. The distributions of the median brightness temperature obtained in a $80'' \times 80''$ region at disk center (beam size $25''$) for Band 6 datasets from 2015 and 2016. The data are separated by antenna, year, and polarization, as labelled. All four basebands (see Table 2) are included as separate values. Note that there were no measurements with PM01 in 2015.

In order to assess the robustness of solar brightness temperatures obtained using Equation (16) with the ALMA calibration measurements, Figures 6 and 7 show the distributions of disk-center brightness temperatures for a number of datasets at Bands 3 and 6, respectively, separating the data by PM antenna, year, and polarization. As far as we know there are no active regions in the low-latitude region around disk center in any of the datasets, so we believe that they should all represent quiet-Sun chromosphere with presumably similar median brightness temperatures, averaged over areas large compared to the typical spatial scales of the network structure likely to be present. We therefore argue that the true brightness temperature at disk center should be very similar in all datasets at a given band, and the spread seen in Figures 6 and 7 represents the level of uncertainty introduced by the calibration scheme. We note that 100 K error is less than 2 % of the absolute temperatures in the range 6000 – 7000 K, but since the goal of the single-dish data is to provide the absolute temperature scale for ALMA solar data, we wish to provide the best possible guidance for solar brightness temperatures.

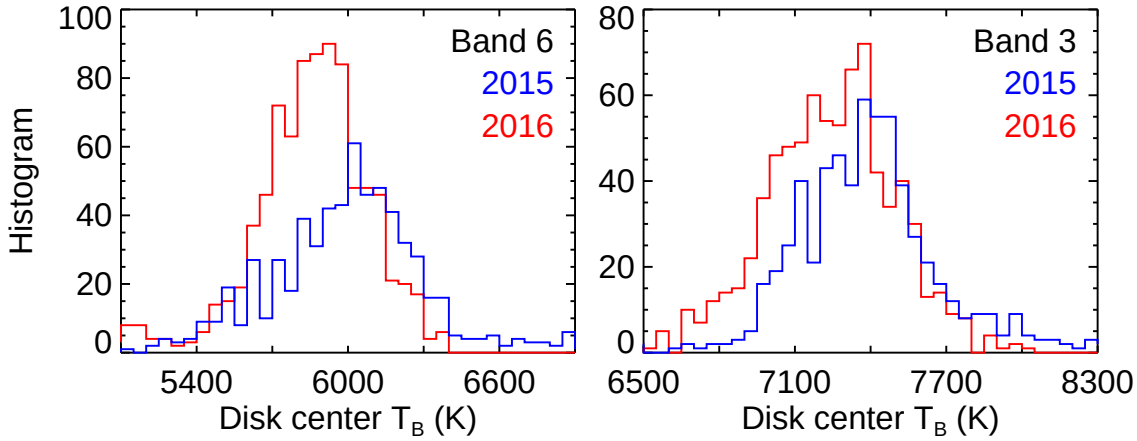

Figure 8. The distributions of the disk center brightness temperatures at Bands 6 (left panel) and 3 (right panel) for all four PM antennas, merged, and excluding datasets known to be bad. The distributions for 2015 (blue) and 2016 (red) are plotted separately.

To that end, in Figure 8 we plot the distributions of brightness temperatures for Bands 3 and 6 in 2015 and 2016, separately, excluding data groups identified as bad from Figures 6 and 7 as described above. We have then fitted Gaussians to the distributions with the results shown in Table 5. In both bands, the

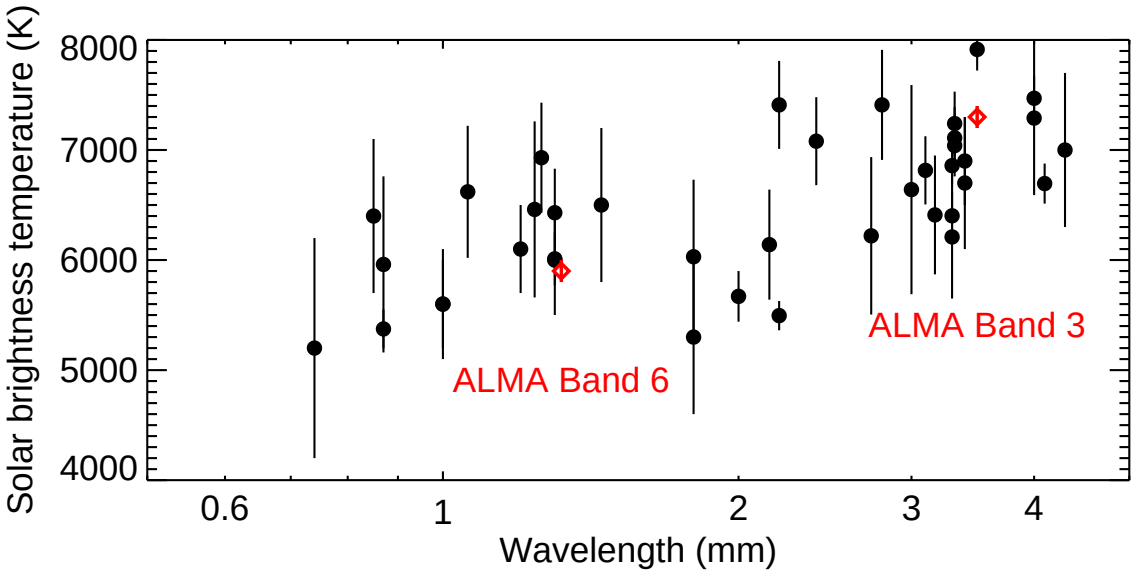

Figure 9. The recommended ALMA disk-center brightness temperatures (red diamonds with ±100 K error bars) at Bands 6 (1.3 mm wavelength) and 3 (3.5 mm), together with previous measurements (black circles with measurement uncertainties) from the compilation by Loukitcheva *et al.* (2015).

values for 2015 are on average about 100 K brighter than in 2016. We are unsure whether this represents a true difference resulting from changes in the chromosphere associated with the lower solar-activity levels in 2016, or whether this is due to the overall uncertainty in the calibration. At higher activity levels, a larger relative contribution of hot network features compared to cooler cell interiors could certainly explain higher quiet-Sun levels at the single-dish spatial resolution. In any case, the central values are sufficiently similar for us to recommend that the quiet-Sun disk-center brightness temperature of the Sun be set to 7300 K at 100 GHz and 5900 K at 230 GHz. The formal standard error in the fitted central values associated with the statistical spread of results is much smaller than the uncertainty of 100 K (≈1.5 %) that we quote: we use that value to account for the difference between the 2015 and 2016 results. The uncertainty of 100 K does not account for the systematic uncertainty associated with the choice of values for $\eta_{\rm l}$ and $\eta_{\rm fss}$ (Table 3), which is much larger (5 %) than this value. Given the large spreads shown in Figure 8, and the uncertainty in the calibration provided by current CASA processing of the single-dish solar data, it is our recommendation that single-dish solar maps should be scaled to these values.

Table 5. Central brightness temperatures and the spread in values for Bands 3 and 6 resulting from fitting Gaussians to the distributions shown in Figure 8. For the first two lines the uncertainty is the Gaussian width of the fit. The third line lists the recommended values for the two bands.

	Band 3	Band 6
2015	7390 ± 220 K	6040 ± 250 K
2016	7280 ± 250 K	5900 ± 190 K
Recommended	7300 ± 100 K	5900 ± 100 K

We can compare these numbers with previous measurements. Loukitcheva *et al.* (2015) provide a compilation of historical brightness temperature measurements of the Sun at millimeter wavelengths. We replot those data here in Figure 9, together with the recommended values from Table 5. Note that the values plotted are not all directly comparable, since different measurements had different spatial resolution and therefore were averaging over different areas of the solar surface. As discussed in the next section, other effects such as limb brightening will also play a role in the measured values: our recommended values apply specifically to quiet-Sun regions at apparent disk center, at the resolution of the ALMA single-dish data. The ALMA values are consistent with previous data, but with much smaller uncertainty due to the large number of values involved in our assessment.

Loukitcheva *et al.* (2015, 2017) use state-of-the-art radiative hydrodynamic simulations of the solar chromosphere (from the Bifrost code; Carlsson *et al.*, 2016) to predict brightness temperatures at millimeter wavelengths. The spatial resolution of the simulations is subarcsecond, and so it is not straightforward to compare their results with the much poorer spatial resolution of the single-dish data. They find average brightness temperatures of 5000 K at 230 GHz and 6200 K at 94 GHz, corresponding to effective heights above the photosphere of about 1150 km at 230 GHz and 1600 km at 94 GHz (Loukitcheva *et al.*, 2017). Earlier simulations of inter-network quiet-Sun regions by Wedemeyer-Böhm *et al.* (2007) found even lower average brightness temperatures. These temperatures are substantially smaller than the values we find here, but detailed comparison requires the use of ALMA interferometer data with a much better match to the spatial resolution of the simulations. If it turns out that the efficiencies quoted in Table 3 are underestimates of the true values, then the brightness temperatures that we determine with the ALMA observations will be reduced.

9.3. Calibration Error Budget

The sources of measurement error in the data required for the application of Equation (16) are as follows:

- The calibration power measurements [$P_{\rm hot}$, $P_{\rm amb}$, $P_{\rm sky}$, and $P_{\rm off}$] have standard deviations about the mean of order 0.1 %. $P_{\rm zero}$ has a larger relative uncertainty, being limited by 16-bit quantization in the measurement, but it always appears as a number to be subtracted from one of the other power measurements, and its uncertainty of order 10^{-4} is at the same absolute level as the other measurements and therefore it too contributes less than 0.1 % to the overall uncertainty.

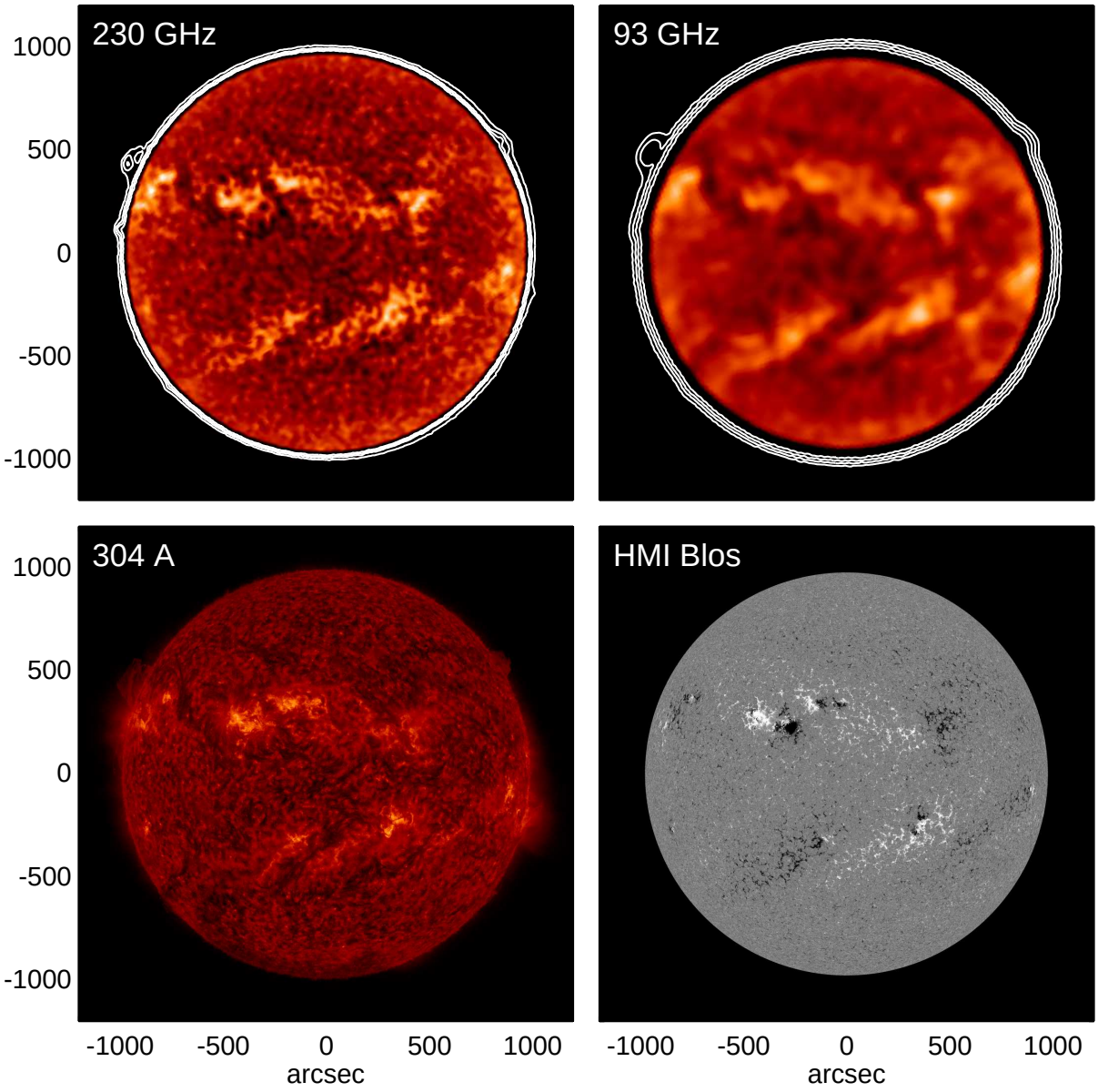

Figure 10. ALMA fast-scanning observations of the Sun on 17 December 2015 at Band 6 (230 GHz at 14:33 UT), upper-left panel) and Band 3 (93 GHz at 18:15 UT, upper-right panel). In order to emphasize structure on the disk, the 230 GHz image color display ranges from 5300 to 7400 K, while the 93 GHz color display ranges from 6700 to 8800 K. Low-level contours are plotted at 300, 600, 1200, and 2400 K in order to show features above the limb. For comparison, we show a *Solar Dynamics Observatory* (SDO) *Atmospheric Imaging Assembly* image of the Sun at 304 Å (lower-left panel, dominated by the HeII line from the upper chromosphere, at 14:44 UT to match 230 GHz), and a line-of-sight magnetogram from the *Helioseismic and Magnetic Imager* (HMI) on board SDO at 18:30 UT (lower-right panel).

- The load temperatures $T_{\rm hot}$ and $T_{\rm amb}$ are measured and their values are present in the datasets. The ALMA technical requirement is an accuracy of 0.3 K for the ambient load and 1.0 K for the hot load (Yagoubov *et al.*, 2011). Inspection of a large number of datasets during the commissioning campaigns showed variability within a 1 K range, consistent with the above requirement and corresponding to an uncertainty of order 0.3 %. The load temperatures can vary within about 10 K of their nominal values, but the actual measured temperatures are used by TELCAL.
- The atmospheric opacity $[\tau]$ is determined by the WVR measurements of the 183 GHz water line in combination with an atmospheric model as described earlier. We do not have a good estimate of the uncertainty in its determination by the ALMA system. Previous studies have compared the opacity measured by a tipper system, usually at 225 GHz, with measurements of PWV and found a spread of

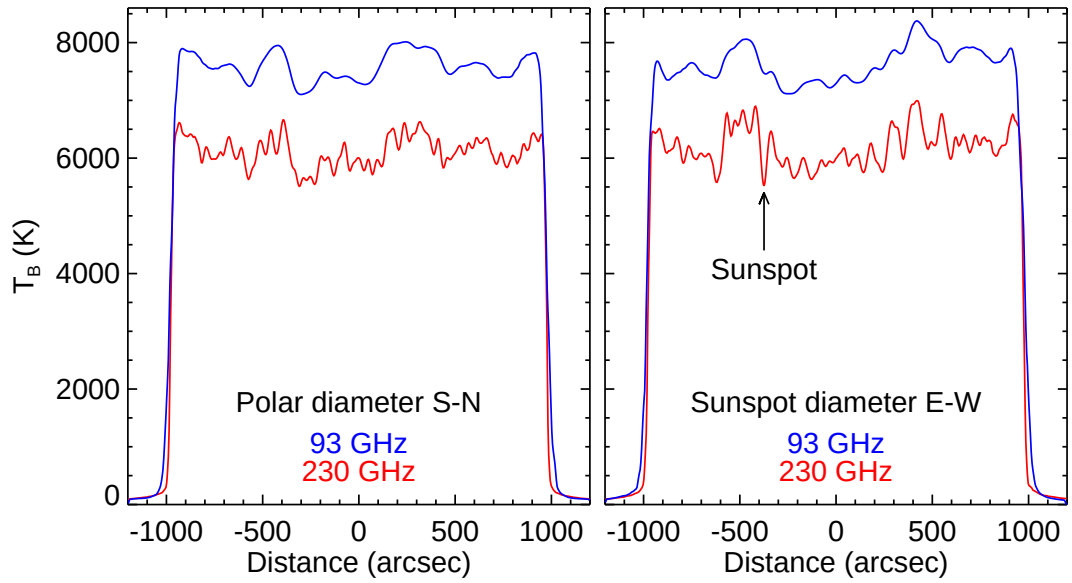

Figure 11. Profiles across the solar disk at 93 (blue) and 230 GHz (red) at two angles: from the South Pole to the North Pole at apparent disk center, and on a diameter through the large sunspot (azimuth 63.8° East of North), from East to West. The 93 GHz image has been rotated back to the time of the 230 GHz image for the comparison. The location of the sunspot in the right panel is marked by an arrow.

order 0.01-0.02 in opacity for a given value of PWV (*e.g.* Chamberlin and Bally, 1995; Delgado *et al.*, 1999). In the calibration expressions τ appears as the factor $\exp(-\tau) \approx 1 - \tau$, and for Bands 3 and 6 typically $\tau < 0.1$ and errors are unlikely to be larger than, say, 0.02. This could give a several percent error in the resulting calibration.

- The uncertainty in the measurements of $P_{\rm src}$ are not well known. We can estimate an upper limit by investigating the variability of the power as the double-circle pattern passes through disk center on each pass: we find again that the variability, much of which is likely to be real solar variability due to oscillation power in the chromosphere (*e.g.* Loukitcheva, Solanki, and White, 2006), is typically less than 2 % for Bands 3 and 6, and the different basebands and polarizations agree to within about 0.1 %. This variability is on the timescale of pattern passes through disk center, which is of the order of a second or less. Fluctuations in atmospheric opacity will also affect $P_{\rm src}$, but they generally have timescales of minutes rather than the millisecond sampling time. Thus we do not expect that the uncertainty in the $P_{\rm src}$ measurements is any worse than in the calibration measurements.

The combined set of uncertainties described above, in particular from the calibration loads and the measurement of τ, yield an uncertainty of order 2-3 %. The 5 % uncertainty in the product $\eta_{\rm l}\,\eta_{\rm fss}$ is an uncertainty in the overall temperature scale: this product could vary from one PM antenna to another and explain differences in the centroids of the individual antenna distributions seen in Figures 6 and 7, but it does not contribute to the spread of results for each individual antenna. The nominal requirement for calibration of ALMA interferometer visibilities is 5 % (P. Yagoubov, private communication). An overall uncertainty in the calibrated temperatures at the few percent level is desirable for quantitative solar work in order to study the energetics of the solar atmosphere, particularly in comparing results at different frequency bands (*e.g.* Wedemeyer *et al.*, 2016).

9.4. Solar Fast-Scanning Images

Representative examples of ALMA fast-scanning images of the Sun from 17 December 2015 are shown in Figure 10. Corresponding examples of ALMA solar interferometer data are presented by Shimojo *et al.* (2017) in a companion paper. The single-dish images in Figure 10 are generated using CASA tasks implementing calibration and gridding as described earlier.[6] The brightness temperature display range is chosen to show

[6]Solar single-dish data should be processed with CASA version 4.7 or later versions.

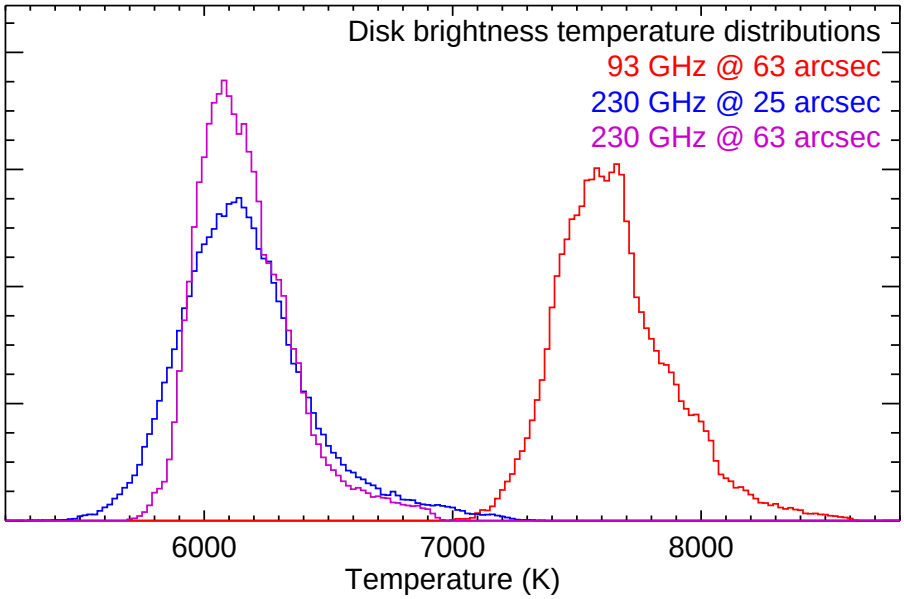

Figure 12. Histograms (arbitrary scale) of temperature distributions on the disk for the images in Figure 10. The plot includes positions out to 90 % of the solar radius. In order to show the likely effects of spatial resolution at 93 GHz, the distribution of 230 GHz temperatures when the image is convolved to the 93 GHz resolution is shown (purple histogram), in addition to the distributions at the native resolution of the 93 GHz (63″, red histogram) and 230 GHz (25″, blue histogram) data.

the full range of brightness temperatures on the disk at Band 6 (left) and Band 3 (right), and lower-level contours are plotted to show off-limb features. For comparison, we show a 304 Å image and a line-of-sight magnetogram from instruments on board the *Solar Dynamics Observatory* (SDO). The 304 Å image is dominated by the HeII line and represents the upper chromosphere. As expected, the bright regions in the ALMA images match the bright regions at 304 Å and the areas of strong magnetic field where additional atmospheric heating would be expected. However, there are obvious differences in the relative brightness of different features: *e.g.* the brightest feature in the south-east quadrant in the ALMA images is not the brightest feature in the same area in the 304 Å image. Further, there are significant differences in the relative brightness of individual features at 230 and 93 GHz, *e.g.* at the same resolution, the active region plage East of the large sunspot is relatively brighter at 230 GHz than at 93 GHz. Prominences visible above the limb in the ALMA images match off-limb emission in the 304 Å image, although again with differences in relative brightness. A large sunspot is present in the north-east quadrant, coincident with the intense negative polarity in the magnetogram. It is clearly visible as a depression surrounded by a bright rim in the 230 GHz image, but it is less obvious at the 60″ resolution of the 93 GHz image. Large-scale cool features are present over filament channels at both ALMA frequencies.

To provide a more quantitative picture of the level of variability across the disk, Figure 11 shows profiles through disk center from both ALMA images along two angles: a polar cut from South to North (left panel), and a diameter at 64° East of North that passes through the large sunspot (right panel). A direct comparison between the 93 and 230 GHz profiles is not possible due to the differing resolutions at the two frequencies: the larger beam at 93 GHz is averaging over about six resolution elements at 230 GHz. The polar cut is dominated by quiet-Sun fluctuations amounting to a few hundred K on small spatial scales. The sunspot diameter crosses a number of bright regions, and in particular the active region encompassing the sunspot, between about −700″ and −300″, which is around 1000 K brighter than the adjacent regions at 230 GHz. The dip in emission over the sunspot umbra is clearly visible in the 230 GHz profile, being less obvious at the resolution of the 93 GHz data: as discussed by Loukitcheva, Solanki, and White (2014), atmospheric models do not predict such a dip in the brightness of the umbra at millimeter wavelengths.

Figure 12 shows histograms of the temperature distributions of the 93 and 230 GHz images in Figure 10 on the disk out to 90 % of the solar diameter. It can be seen that the 230 GHz temperatures range from 5400 K up to 7300 K, while the 93 GHz temperatures range from 7000 to 8600 K. The larger temperature range at 230 GHz (almost 2000 K) is likely a function of spatial resolution: when convolved to the 63″ resolution of the 93 GHz map (purple histogram in Figure 12), the range of temperatures reduces to 5700 – 7000 K.

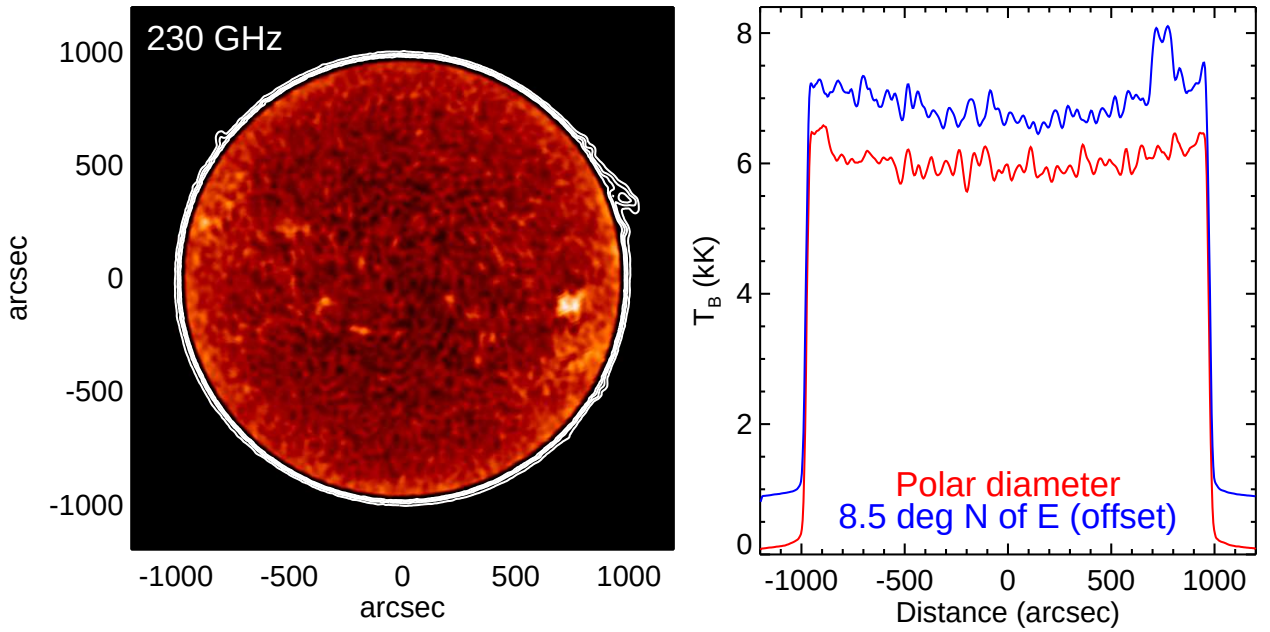

Figure 13. A 230 GHz image of the Sun on 7 December 2016, at a much lower activity state than in Figure 10. The display range and the contours in the left panel are identical to those of the 230 GHz image in Figure 10. The right panel shows disk profiles through the Poles and on a diameter through the active region in the southwest quadrant, but with the blue curve offset by 800 K in order to show structure in both.

The "recommended" temperatures for quiet-Sun at disk center are on the low side of the histograms in both cases, as expected with the large area of more active Sun present on the disk.

By contrast, Figure 13 shows a 230 GHz image from a year later at a much lower level of solar activity. Only one active region is visible on the disk, and again it is almost 1000 K brighter than the surrounding quiet Sun. In this case the profiles across the disk show much lower levels of variability. The quiet-Sun network structure is very prominent in this image, and the contrast between network and cell interiors dominates the variability on small spatial scales. Prominences above the limb are again readily visible. In addition, there is clear evidence for limb brightening in this image, which might also be present in the 2015 data but could be masked there by the higher overall level of activity.

Unfortunately, these images are not sufficient to study the limb brightening and compare with chromospheric models because they are convolved with the point-spread response of the single-dish telescope, which has broad wings: the effects of these wings are evident in the relatively smooth fall-off of emission above the limb (beyond 1000″ from disk center) in Figures 11 and 13. The wings of the point-spread function (PSF) will play a role in the apparent amount of limb brightening, and deconvolution of the PSF from the images is required for quantitative analysis. This effect will be addressed in a future study.

10. Conclusions

We have described solar single-dish imaging using the fast-scanning technique implemented on 12 m ALMA dishes. The results of commissioning are summarized, leading to the availability of single-dish maps to supplement ALMA interferometer observations of the Sun. The single-dish data provide the absolute temperature scale missing from the interferometer data, and can be used to fill in the large-scale structure when deconvolving mosaic images (*e.g.* Shimojo *et al.*, 2017). The observations are carried out in a "detuned" receiver mode in which the mixers are biassed to a level that provides a lower gain with a more linear response over the full temperature range appropriate to the Sun. A calibration path using all five calibration power measurements, together with atmospheric properties from the WVR and the "forward" [η_l] and "forward scattering and spillover" [$\eta_{\rm fss}$] antenna efficiencies, is shown to be successful in determining the solar temperature. This calibration path is not yet implemented in CASA. The uncertainty in the calibration of individual datasets is larger than is desirable for solar applications, and we recommend that the standard ALMA single-dish image products be scaled to match our best determination of quiet-Sun temperatures

at disk center (specifically, 5900 K averaged over an 80″-square region centered on apparent disk center at Band 6, and 7300 K averaged over a 120″-square region centered on apparent disk center at Band 3, with uncertainties of order 100 K) while work continues to understand the source of this variation. There is uncertainty in the exact values of the two antenna efficiencies required for calibration, which affects the scaling of the data and the recommended values above, and better measurements of these properties may be available in the future.

Analysis of sample images shows that the temperature on the disk can vary over about a 2000 K range at the 25″ resolution of the Band 6 data: this implies that an even larger range of variation should be seen in the sub-arcsecond interferometer images. Active regions, plage, sunspot umbrae, prominences, and filament channels are all strikingly present in the images, demonstrating the range of features and properties of the solar atmosphere that ALMA will study.

Acknowledgments The ALMA solar commissioning effort was supported by ALMA Development grants from NRAO (for the North American contribution), ESO (for the European contribution) and NAOJ (for the East Asia contribution). The help and cooperation of the ALMA Extension and Optimization of Capabilities (EOC) team as well as the engineers, telescope operators, astronomers-on-duty and staff at the ALMA Operations Support Facility was crucial for the success of solar commissioning campaigns in 2014 and 2015. We are grateful to the ALMA project for making solar observing with ALMA possible. R. Brajša acknowledges partial support of this work by Croatian Science Foundation under the project 6212 Solar and Stellar Variability and by the European Commission FP7 project SOLARNET (312495, 2013 - 2017), which is an Integrated Infrastructure Initiative (I3) supported by the FP7 Capacities Programme. G. Fleishmann acknowledges support from NSF grants AGS-1250374 and AGS-1262772. Travel by Y. Yan to ALMA for the 2015 commissioning campaign was partially supported by NSFC grant11433006.

Disclosure of Potential Conflicts of Interest

The authors declare that they have no conflicts of interest affecting this article.

References

Bastian, T.S., Ewell, M.W., Zirin, H.: 1993, The center-to-limb brightness variation of the sun at lambda = 850 microns. *Astrophys. J.* **415**, 364. DOI. ADS.

Brajša, R., Benz, A.O., Temmer, M., Jurdana-Šepić, R., Šaina, B., Wöhl, H.: 2007, An Interpretation of the Coronal Holes' Visibility in the Millimeter Wavelength Range. *Solar Phys.* **245**, 167. DOI. ADS.

Brogan, C.L., Hunter, T.R.: 2014, ALMA Single–Dish Imaging Parameters, *NAASC Memo 114 (draft)*.

Broguière, D., Lucas, R., Pardo, J., Roche, J.-C.: 2011, TELCAL: The On-line Calibration Software for ALMA. In: Evans, I.N., Accomazzi, A., Mink, D.J., Rots, A.H. (eds.) *Astronomical Data Analysis Software and Systems XX*, **CS-442**, Astron. Soc. Pacific, San Francisco, 277. ADS.

Buhl, D., Tlamicha, A.: 1970, The Mapping of the Sun at 3.5 MM. *Astron. Astrophys.* **5**, 102. ADS.

Carlsson, M., Hansteen, V.H., Gudiksen, B.V., Leenaarts, J., De Pontieu, B.: 2016, A publicly available simulation of an enhanced network region of the Sun. *Astron. Astrophys.* **585**, A4. DOI. ADS.

Casalta, J.M., Molins, A., Bassas, M., Canchado, M., Creus, E., Tomàs, A.: 2008, ALMA front end amplitude calibration device design and measured performances. In: *Advanced Optical and Mechanical Technologies in Telescopes and Instrumentation*, *Proc. IEEE* **7018**, 701838. DOI. ADS.

Chamberlin, R.A., Bally, J.: 1995, The observed relationship between the south pole 225-GHz atmospheric opacity and the water vapor column density. *International Journal of Infrared and Millimeter Waves* **16**, 907. DOI. ADS.

Clark, T.A., Naylor, D.A., Tompkins, G.J., Duncan, W.D.: 1992, Extension of the solar limb and sub-millimeter and millimeter wavelengths. *Solar Phys.* **140**, 393. DOI. ADS.

Coates, R.J.: 1958,. *Proc. IRE* **46**, 122.

Delgado, G., Otárola, A., Belitsky, V., Urbain, D.: 1999, The Determination of Precipitable Water Vapour at Llano de Chajnantor from Observations of the 183 GHz Water Line. *ALMA Memo 271*, Joint ALMA Observatory, Santiago.

Ekers, R.D., Rots, A.H.: 1979, Short Spacing Synthesis from a Primary Beam Scanned Interferometer. In: van Schooneveld, C. (ed.) *IAU Colloq. 49: Image Formation from Coherence Functions in Astronomy*, D. Reidel, Dordrecht, 61. DOI. ADS.

Hills, R.E.: 2016, PM Antenna Servo Characterization. *ALMA CSV-3243 Report*.

Hills, R.E.: 2010, Correcting for the Effects of the Atmosphere. *ALMA Newsletter* **6**, ESO, Garching, 2. ADS.

Iguchi, S., Morita, K.-I., Sugimoto, M., Vila Vilaró, B., Saito, M., Hasegawa, T., Kawabe, R., Tatematsu, K., Seiichi, S., Kiuchi, H., Okumura, S.K., Kosugi, G., Inatani, J., Takakuwa, S., Iono, D., Kamazaki, T., Ogasawara, R., Ishiguro, M.: 2009, The Atacama Compact Array (ACA). *Publ. Astron. Soc. Japan* **61**, 1. DOI. ADS.

Iwai, K.: 2016a, Fast Scan Pattern Simulation. *ALMA CSV-3244 Solar Commissioning Report*.

Iwai, K.: 2016b, Nonlinearity of ALMA Antennas in Detuning Mode 1. *ALMA CSV-3246 Solar Commissioning Report*.

Iwai, K., Shimojo, M.: 2015, Observation of the Chromospheric Sunspot at Millimeter Range with the Nobeyama 45 m Telescope. *Astrophys. J.* **804**, 48. DOI. ADS.

Jewell, P.R.: 2002, Millimeter Wave Calibration Techniques. In: Stanimirovic, S., Altschuler, D., Goldsmith, P., Salter, C. (eds.) *Single-Dish Radio Astronomy: Techniques and Applications*, **CS-278**, Astron. Soc. Pacific, San Francisco, 313. ADS.

Kaufmann, P., Strauss, F.M., Schaal, R.E., Laporte, C.: 1982, The use of the large mm-wave antenna at itapetinga in high-sensitivity solar research. *Solar Phys.* **78**, 389. DOI. ADS.

Koda, J., Scoville, N., Sawada, T., La Vigne, M.A., Vogel, S.N., Potts, A.E., Carpenter, J.M., Corder, S.A., Wright, M.C.H., White, S.M., Zauderer, B.A., Patience, J., Sargent, A.I., Bock, D.C.J., Hawkins, D., Hodges, M., Kemball, A., Lamb, J.W., Plambeck, R.L., Pound, M.W., Scott, S.L., Teuben, P., Woody, D.P.: 2009, Dynamically Driven Evolution of the Interstellar Medium in M51. *Astrophys. J. Letters* **700**, L132. DOI. ADS.

Kosugi, T., Ishiguro, M., Shibasaki, K.: 1986, Polar-cap and coronal-hole-associated brightenings of the sun at millimeter wavelengths. *Publ. Astron. Soc. Japan* **38**, 1. ADS.

Kundu, M.R.: 1970, Solar active regions at millimeter wavelengths. *Solar Phys.* **13**, 348. DOI. ADS.

Kutner, M.L., Ulich, B.L.: 1981, Recommendations for calibration of millimeter-wavelength spectral line data. *Astrophys. J.* **250**, 341. DOI. ADS.

Labrum, N.R.: 1978, Evidence on chromospheric structure from observations of solar brightness distribution at millimeter wavelengths. *Proc. Astron. Soc. Austr.* **3**, 256. ADS.

Lindsey, C., Hudson, H.S.: 1976, Solar limb brightening in submillimeter wavelengths. *Astrophys. J.* **203**, 753. DOI. ADS.

Linsky, J.L.: 1973a, A recalibration of the quiet sun millimeter spectrum based on the moon as an absolute radiometric standard. *Solar Phys.* **28**, 409. DOI. ADS.

Linsky, J.L.: 1973b, The Moon as a Proposed Radiometric Standard for Microwave and Infrared Observations of Extended Sources. *Astrophys. J. Supp.* **25**, 163. DOI. ADS.

Loukitcheva, M., Solanki, S.K., White, S.M.: 2006, The dynamics of the solar chromosphere: comparison of model predictions with millimeter-interferometer observations. *Astron. Astrophys.* **456**, 713. DOI. ADS.

Loukitcheva, M., Solanki, S.K., White, S.M.: 2014, The chromosphere above sunspots at millimeter wavelengths. *Astron. Astrophys.* **561**, A133. DOI. ADS.

Loukitcheva, M., Solanki, S.K., Carlsson, M., White, S.M.: 2015, Millimeter radiation from a 3D model of the solar atmosphere. I. Diagnosing chromospheric thermal structure. *Astron. Astrophys.* **575**, A15. DOI. ADS.

Loukitcheva, M., White, S.M., Solanki, S.K., Fleishman, G.D., Carlsson, M.: 2017, Millimeter radiation from a 3D model of the solar atmosphere. II. Chromospheric magnetic field. *Astron. Astrophys.* in press.

Lucas, R.: 2012, Temperature Scale Calibration. *Unpublished talk for ALMA staff.*

Mangum, J.: 2002, Load calibration at millimeter and submillimeter wavelengths. *ALMA Memo 434*, Joint ALMA Observatory, Santiago.

Mangum, J.G.: 1993, Main-beam efficiency measurements of the Caltech Submillimeter Observatory. *Publ. Astron. Soc. Pacific* **105**, 117. DOI. ADS.

Mangum, J.G., Emerson, D.T., Greisen, E.W.: 2007, The On The Fly imaging technique. *Astron. Astrophys.* **474**, 679. DOI. ADS.

Newstead, R.A.: 1969, Solar limb brightening and enhancement measurements at 1.2 mm. *Solar Phys.* **6**, 56. DOI. ADS.

Nikolic, B., Bolton, R.C., Graves, S.F., Hills, R.E., Richer, J.S.: 2013, Phase correction for ALMA with 183 GHz water vapour radiometers. *Astron. Astrophys.* **552**, A104. DOI. ADS.

Noyes, R.W., Beckers, J.M., Low, F.J.: 1968, Observational studies of the solar intensity profile in the far infrared and millimeter regions. *Solar Phys.* **3**, 36. DOI. ADS.

Pardo, J.R., Cernicharo, J., Serabyn, E.: 2001, Atmospheric Transmission at Microwaves (ATM): An Improved Model for Millimeter/Submillimeter Applications. *IEEE Trans. Antenn. Prop.* **49**, 1683. DOI. ADS.

Phillips, N., Hills, R., Bastian, T., Hudson, H., Marson, R., Wedemeyer, S.: 2015, Fast Single-Dish Scans of the Sun Using ALMA. In: Iono, D., Tatematsu, K., Wootten, A., Testi, L. (eds.) *Revolution in Astronomy with ALMA: The Third Year*, **CS-499**, Astron. Soc. Pacific, San Francisco, 347. ADS.

Righini, G., Simon, M.: 1976, Solar brightness distribution at 350 and 450 microns. *Astrophys. J.* **203**, L95. DOI. ADS.

Shimojo, M., Bastian, T.S., Hales, A., and 24 other authors: 2017, Observing the Sun with ALMA: High Resolution Interferometric Imaging. *Solar Phys.* in press.

Sinton, W.M.: 1952, Detection of Millimeter Wave Solar Radiation. *Phys. Rev.* **86**, 424. DOI. ADS.

Sugimoto, M., Kosugi, G., Iguchi, S., Iwashita, H., Saito, M., Inatani, J., Takahashi, T., Tasaki, M., Nakanishi, K., McMullin, J.P., Puga, J.P., Hoff, B., Norambuena, J., Kamazaki, T., Vila-Vilar, B., Ikenoue, B., Morita, K.-I., Asayama, S., Yamada, M., Kiuchi, H.: 2009, Beam Pattern Measurements and Observational Evaluations of the ALMA/ACA 12-m Antenna. *Publ. Astron. Soc. Japan* **61**, 451. DOI. ADS.

Tamura, Y., Sugimoto, M.: 2012, Preliminary Analysis of the Forward Efficiency. *ALMA System Verification Report SYS #132*, Joint ALMA Observatory, Santiago.

Tolbert, C.W., Straiton, A.W.: 1961, Solar emission at millimeter wavelengths. *Astrophys. J.* **134**, 91. DOI. ADS.

Ulich, B.L., Haas, R.W.: 1976, Absolute calibration of millimeter-wavelength spectral lines. *Astrophys. J. Supp.* **30**, 247. DOI. ADS.

Urpo, S., Krüger, A., Hildebrandt, J.: 1986, Millimetre wave sources in the solar corona. *Astron. Astrophys.* **163**, 340. ADS.

van Kempen, T., Corder, S., Lucas, R., Mauersberger, R.: 2012, How ALMA is calibrated. *ALMA Newsletter* **9**, ESO, Garching, 8. ADS.

Vernazza, J.E., Avrett, E.H., Loeser, R.: 1976, Structure of the solar chromosphere. ii. the underlying photosphere and temperature-minimum region. *Astrophys. J. Supp.* **30**, 1. DOI. ADS.

Vršnak, B., Pohjolainen, S., Urpo, S., Terasranta, H., Brajša, R., Ruždjak, V., Mouradian, Z., Jurac, S.: 1992, Large-scale patterns on the sun observed in the millimetric wavelength range. *Solar Phys.* **137**, 67. DOI. ADS.

Warmels, R., Remijan, A.J.: 2017, ALMA Cycle 5 Technical Handbook, Joint ALMA Observatory, Santiago.

Wedemeyer, S., Bastian, T., Brajša, R., Hudson, H., Fleishman, G., Loukitcheva, M., Fleck, B., Kontar, E.P., De Pontieu, B., Yagoubov, P., Tiwari, S.K., Soler, R., Black, J.H., Antolin, P., Scullion, E., Gunár, S., Labrosse, N., Ludwig, H.-G., Benz, A.O., White, S.M., Hauschildt, P., Doyle, J.G., Nakariakov, V.M., Ayres, T., Heinzel, P., Karlicky, M., Van Doorsselaere, T., Gary, D., Alissandrakis, C.E., Nindos, A., Solanki, S.K., Rouppe van der Voort, L., Shimojo, M., Kato, Y., Zaqarashvili, T., Perez, E., Selhorst, C.L., Barta, M.: 2016, Solar Science with the Atacama Large Millimeter/Submillimeter Array - A New View of Our Sun. *Space Sci. Revs.* **200**, 1. DOI. ADS.

Wedemeyer-Böhm, S., Ludwig, H.G., Steffen, M., Leenaarts, J., Freytag, B.: 2007, Inter-network regions of the Sun at millimetre wavelengths. *Astron. Astrophys.* **471**, 977. DOI. ADS.

White, S.M.: 1999, Radio versus euv/x–ray observations of the solar atmosphere. *Solar Phys.* **190**, 309. DOI. ADS.
Whitehurst, R.N., Copeland, J., Mitchell, F.H.: 1957, Solar Radiation and Atmospheric Attenuation at 6-Millimeter Wavelength. *J. App. Phys.* **28**, 295. DOI. ADS.
Wootten, A., Thompson, A.R.: 2009, The Atacama Large Millimeter/Submillimeter Array. *IEEE Proc.* **97**, 1463. DOI. ADS.
Yagoubov, P.A.: 2013, Solar observations with ALMA - How to minimize saturation in SIS mixers. In: *38th International Conference on Infrared, Millimeter, and Terahertz Waves*, IEEE, New York, 1. DOI. ADS.
Yagoubov, P.A., Murk, A., Wylde, R., Bell, G., Tan, G.H.: 2011, Calibration loads for ALMA. In: *36th International Conference on Infrared, Millimeter, and Terahertz Waves*, IEEE, New York, 1. DOI.